# Integrative *in vivo* analysis of the ethanolamine utilization bacterial microcompartment in *Escherichia coli*.

**Running title: *In vivo* functionality of the *E. coli* Eut BMC**

Denis Jallet[1#], Vanessa Soldan[2], Ramteen Shayan[2], Alexandre Stella[3,5], Nour Ismail[1], Rania Zenati[1], Edern Cahoreau[1,4], Odile Burlet-Schiltz[3,5], Stéphanie Balor[2], Pierre Millard[1,4], Stéphanie Heux[1].

[1] Toulouse Biotechnology Institute, Université de Toulouse, CNRS, INRAE, INSA, Toulouse, France

[2] Plateforme de Microscopie Electronique Intégrative, Centre de Biologie Intégrative, Université de Toulouse, CNRS, Toulouse, France

[3] Institut de Pharmacologie et de Biologie Structurale (IPBS), Université de Toulouse, CNRS, Université Toulouse III – Paul Sabatier (UT3), Toulouse, France

[4] MetaToul-MetaboHUB, National infrastructure of metabolomics and fluxomics, Toulouse, France

[5] Infrastructure nationale de protéomique, ProFI, FR 2048, Toulouse, France

# Correspondance: denis.jallet@insa-toulouse.fr

## Abstract

Bacterial microcompartments (BMCs) are self-assembling protein megacomplexes that encapsulate metabolic pathways. Although approximately 20% of sequenced bacterial genomes contain operons encoding putative BMCs, few have been thoroughly characterized, nor any in the most studied *Escherichia coli* strains. We used an interdisciplinary approach to gain deep molecular and functional insights into the ethanolamine utilization (Eut) BMC system encoded by the *eut* operon in *E. coli* K-12. The *eut* genotype was linked with the ethanolamine utilization phenotype using deletion and overexpression mutants. The subcellular dynamics and morphology of the *E. coli* Eut BMC were characterized *in cellula* by fluorescence microscopy and electron (cryo)microscopy. The minimal proteome reorganization required for ethanolamine utilization and the *in vivo* stochiometric composition of the Eut BMC were determined by quantitative proteomics. Finally, the first flux map connecting the Eut BMC with central metabolism *in cellula* was obtained by genome scale modelling and $^{13}$C-fluxomics. Our results reveal that, contrary to previous suggestions, ethanolamine serves both as a nitrogen and a carbon source in *E. coli* K-12, while also contributing significant metabolic overflow. Overall, this study provides a quantitative molecular and functional understanding of the BMCs involved in ethanolamine assimilation by *E. coli*.

## Importance

The properties of BMCs make them an ideal tool to build orthogonal network structures with minimal interactions with native metabolic and regulatory networks. However, this requires an understanding of how BMCs work natively. In this study, we combined genetic manipulation, multi-omics, modelling and microscopy to address this issue for Eut BMCs. We show that the Eut BMC in *E. coli* turns ethanolamine into usable carbon and nitrogen substrates to sustain growth. These results improve our understanding of compartmentalization in a widely used bacterial chassis.

## Introduction

Compartmentalization was initially considered a defining feature of eukaryotic cells. With the advent of transmission electron microscopy (TEM) however, subcellular structures were also discovered in bacteria, including bacterial microcompartments (BMCs) such as carboxysomes in certain autotrophic taxa[1]. Genes encoding for BMC shell proteins were subsequently discovered in heterotrophic taxa[2,3] and recent isolate and metagenomics data suggest that roughly 20% of bacteria have BMC encoding operons[4]. These genes are generally found in large operons with the other genetic components required to produce BMCs, often referred to as metabolosomes, because of their typically catabolic rather than anabolic function. The ethanolamine utilization (Eut) BMC in *Salmonella enterica* was one of the first studied metabolosome systems[5].

Ethanolamine (EA) accumulates in mammalians' gastrointestinal and urinary tracts upon degradation of phosphatidylethanolamine. EA utilization confers competitive advantages to certain pathogenic bacteria in the gut environment[6–8]. Some *Escherichia coli* strains can utilize EA as sole nitrogen and carbon source in the presence of vitamin B12[6,9–12]. EA utilization was initially thought to be associated with pathogenicity[6,13] but several commensal *E. coli* strains also metabolize EA[11,12]. The *E. coli* core genome natively hosts a 17-gene *eut* operon (*eutSPQTDMNEJGHABCLKR*) with strong homology to the *eut* operon of *S. enterica*[14,15]. Other genes, such as *maeB, talA or tktB*, flank the *eut* operon to form an extended EUT1 locus[16,17]. The EUT1 locus is well conserved amongst various Beta- and Gammaproteobacteria[4], suggesting a functional link between at least some of these ancillary EUT1 proteins and EA utilization[16]. However, the link has not been evaluated experimentally yet. EUT loci with different *eut* operon arrangements and ancillary gene contents also exist amongst bacteria (i.e. EUT2 and EUT3 loci[4,16]). Since *E. coli* only has an EUT1 locus, EUT1 will be the focus of the present study.The *eut* operon contains genes encoding for BMC components. The Eut BMC shell is made up of ring-shaped oligomeric proteins (EutSMNLK), some of which have central pores that allow some small metabolites to pass, including EA and its degradation products[18]. Inside Eut BMCs, EA is thought to be deaminated into acetaldehyde plus ammonium ($NH_4$) by EAL (EutBC), but the exact metabolic topology involved remains debated[19,20]. Acetaldehyde is further converted through enzymatic reactions. $NH_4$, ethanol and acetyl-P would eventually diffuse out through the shell to be used in central metabolism or excreted[19]. But again, the exact BMC core protein complement remains hypothetical. Two Eut enzymes (EutC, EutE) bear encapsulation peptides that likely favour their internalization[21,22]. Other Eut enzymes may form complexes or interact with shell components.

Electron micrographs of *E. coli* Eut BMCs have only ever been reported twice[9,23]. Indeed, while irregular polyhedral structures with a diameter of around 100 nm can be observed in *E. coli* K-12 and *E. coli* UPEC U1 after *eut* induction, it is unclear whether these Eut BMCs are well formed and functionally required for EA catabolism. Intact Eut BMCs have never been purified to date, either from *E. coli* or from *S. enterica*, and our knowledge of these systems mainly comes from genetic studies in *S. enterica*[19,20,24] and *in vitro* structural and functional characterizations of individual recombinant Eut proteins[18].

Overall, Eut BMCs play a safeguarding role by sequestering and favouring the downstream conversion of toxic and volatile acetaldehyde intermediates[20]. Their spatial arrangement favours metabolic channelling and it has been reported that compartmentalisation may increase catalytic activity by up to 6-fold compared with non-compartmentalised reactions[25]. Another advantage is that the cofactors required for enzyme activity are regenerated within the BMC thus limiting competition with enzymes from the cytosol[19]. These properties make Eut BMCs and BMCs interesting metabolic units for biotechnological applications[26], but a better understanding of their regulation, assembly and function is still required to make them amenable to engineering. With these knowledge gaps in mind, we

performed a systemic analysis from the molecular to the functional level of native BMC-mediated EA catabolism in *E. coli* K-12. We characterized wild-type (WT) *E. coli* K-12 W3110 and several mutant strains by epifluorescence microscopy, TEM and electron cryotomography (cryoET) and performed a multi omics analysis to understand how BMC-mediated EA utilization affects bacterial physiology.

## Results

### *1) Necessity of the eut operon for EA utilization.*

The EUT1 locus of *E. coli* K-12 W3110 (Fig.1A) is similar in gene content to *S. enterica* LT2's, with more than 73 % primary structure identity between individual EUT1 proteins from the two species (Table S2). In contrast, the *eut* operon of *E. coli* K-12 BW25113 is natively interrupted by a prophage DNA insertion downstream of *eutA* (Fig.S1A). *E. coli* K-12 does not contain any other putative BMC locus besides EUT1 (e.g. no PDU locus). To investigate the link between *eut* genotype and EA catabolism, we first constructed several mutant strains by genome editing[27]. The *eut* operon was knocked out from WT W3110 to yield W3110 Δ*eut* (Table 1; Fig.S1B). The prophage DNA insertion in BW25113 WT was scarlessly removed to reconstitute an intact *eut* operon, thereby generating BW25113 *eut+*. We additionally built *eut* overexpressors by cloning the entire W3110 WT *eut* operon downstream of an IPTG-inducible promoter ($P_{trc}$[28]) in pSEVA661[29], yielding pEut (Fig.S1C). pEut was transformed into W3110 Δ*eut* for complementation assays.

Growth experiments were performed using a microplate reader to evaluate each strain's EA utilization capacity. The W3110 strains (WT and Δ*eut*) behaved similarly in control M9 medium with glycerol as C source and $NH_4Cl$ as N source (Fig.1B). However, only the WT strain grew in M9 glycerol EA B12, where EA was the only available N source (Fig.1C). W3110 WT had comparable growth rates (Table 2) but significantly higher $OD_{600nm}$ after 24 h in M9 glycerol EA B12 than in M9 glycerol $NH_4Cl$ (0.73 ± 0.01 VS 0.56 ± 0.04). BW25113 WT behaved like W3110 Δ*eut* and BW25113 *eut+* behaved like W3110 WT (Fig.S1D-E), indicating that an uninterrupted *eut* operon is essential for EA utilization as N source. Note that none of the strains grew in M9 EA B12 where EA was the only available N and C source (Fig.S1F). In M9 glycerol $NH_4Cl$ with gentamicin (Gm), W3110 Δ*eut* pEut's growth rate was similar to that of the empty-vector control (W3110 Δ*eut* pO) and of the corresponding plasmid-bearing WT derivatives (Table 2; Fig.1B). W3110 Δ*eut* pO did not grow in M9 glycerol EA B12 Gm (Fig.1C) while W3110 Δ*eut* pEut utilized EA as sole N source with a maximal growth rate similar to that of W3110 WT pO (Table 2) but with a markedly lower final $OD_{600nm}$ (0.60 ± 0.01 VS 0.77 ± 0.01). The W3110 *eut* phenotype was thus at least partially recovered in the plasmid construct, even without IPTG induction, which indicates that the $P_{trc}$ promoter is leaky. When 20 µM IPTG was added at culture initiation, W3110 WT pEut and W3110 Δ*eut* pEut had significantly lower growth rates than the empty vector controls in both M9 glycerol $NH_4Cl$ Gm and M9 glycerol EA B12 Gm (Fig.1D,E; Table 2). These results show that *eut* expression levels must be kept low to avoid any negative impact on growth and enable efficient EA utilization.

### *2) Subcellular localization of the EutC enzyme.*

The EUT1 locus encodes a functional EA utilization pathway but does it truly drive the production of Eut BMCs *in cellula*? We first attempted to visualize *E. coli* Eut BMCs by fluorescence microscopy and EutC-GFP fusion. We focused on EutC because it natively carries a 20 amino-acid long N-terminal peptide (referred to as $EutC_{1-20}$ hereafter) that should ensure its encapsulation within BMCs[21,22]. To keep expression levels low, the synthetic gene was inserted at the SS9 safe chromosomal locus[30] (Table 1; Fig2A) in W3110 WT under the control of an anhydrotetracycline (aTc) inducible promoter ($P_{LtetO-1}$[31]).

No GFP fluorescence emission was detected in the absence of aTc (Fig.S2A). In M9 glycerol $NH_4Cl$ with 8 ng.ml$^{-1}$ aTc, a faint cytosolic GFP signal was observed (Fig.2B). In M9 glycerol EA B12 with 8 ng.ml$^{-1}$ aTc, multiple GFP puncta were observed moving rapidly around the cytosol (Fig.2C; Movie S1; wider views in Fig.S3). These mobile GFP puncta are similar to those visualized by fluorescence microscopy for the *S. enterica* Eut BMC system[21,32]. There were 5.9 ± 1.1 GFP puncta per bacterium on average, a number that did not vary significantly upon increasing the aTc concentration up to 80 ng.ml$^{-1}$ (6.3 ± 1.2) (Fig.2D,E). To investigate whether $EutC_{1-20}$ alone could drive the encapsulation of a heterologous protein, we also built a smaller cassette expressing the $EutC_{1-20}$-GFP fusion protein (Fig.S2B). W3110 *eut$C_{1-20}$-GFP* behaved like W3110 *eutC-GFP* but with a stronger cytosolic GFP background (Fig.S2C-E), making it harder to distinguish the puncta. The diffuse GFP background in W3110 *eut$C_{1-20}$-GFP* likely came from non-encapsulated $EutC_{1-20}$-GFP fusions.

*3) Morphology of Eut BMCs in cellula.*

We first used a traditional TEM-based approach to evaluate the integrity of the Eut BMCs *in cellula*. No BMC-like structure was detected in W3110 WT growing in M9 glycerol $NH_4Cl$ (Fig.S4A). In M9 glycerol EA B12, irregular polyhedral assemblies roughly 100 nm in diameter, with sharp edges and a well-defined delimiting layer were observed in some slices (Fig. S4B). Since these assemblies satisfy the morphological criteria for BMCs[33] we refer to them hereafter as Eut BMCs. These were present in about 1 in 50 bacterial slices. On LB medium supplemented with EA and vitamin B12 to induce *eut*, Eut BMCs were detected in about 1 in 10 bacterial slices (Fig.S4C) suggesting that more BMCs were present. Finally, W3110 Δ*eut* pEut was cultivated in LB containing IPTG to strongly induce the *eut* operon expression. Here, BMCs with various polyhedral geometries and dimensions were observed in most bacteria (Fig.S4D). Increasing the *eut* operon expression strength thus increased the number of BMCs per bacterium but had a negative effect on growth.

CryoET reconstructions of W3110 WT grown in M9 glycerol EA B12 revealed several cellular features including the inner and outer membranes, ribosomes, and Eut BMCs (Fig.3A-B). Multiple Eut BMCs were observed per bacterium, surrounded by a thin layer (the BMC shell) with sharp edges and vertices (Fig.3C-D). The shell often completely enclosed the core but structures resembling partial Eut BMCs were also present (arrow in Fig.3D). Further experiments are required to determine whether these apparently partial Eut BMCs correspond to (dis)assembling states or are in fact cryoET (e.g. missing wedge) artefacts. The Eut BMC core was somewhat granular in appearance but more electron dense than the surrounding cytoplasm, with several encapsulated components, likely proteins. This was particularly apparent in bacteria with a clear cytosol after partial lysis (Fig.3D). Overall, these *E. coli* Eut BMCs were more heterogenous in size and shape than cyanobacterial carboxysomes[34]. Tomograms of the W3110 Δ*eut* pEut strain cultivated in M9 glycerol EA B12 Gm IPTG as a control showed a higher number of Eut BMCs per bacterium compared with the WT (Fig.3E-F; Fig.S5), but with similar shapes and dimensions. These first ever cryoET images of Eut BMCs in a bacterium demonstrate that native *E. coli* Eut BMCs are properly formed.

*4) EA utilization requires minimal reorganization of the proteome.*

Since Eut BMCs are protein-based, we investigated how their production affects *E. coli* using label-free quantitative mass spectrometry-based proteomics. Samples were collected and compared between exponentially growing cultures of W3110 WT maintained aerobically in M9 glycerol EA B12 versus M9 glycerol $NH_4Cl$. Of the 1999 quantifiable proteins, only 48 were significantly more abundant and 8 less abundant in M9 glycerol EA B12 compared with M9 glycerol $NH_4Cl$ (Fig.4A; Table S3). Two distinct modules were identified among these proteins by interaction network analysis using STRING v11.5[35] (Fig.4B).

Some of the *eut* encoded proteins in the first module were detected in M9 glycerol EA B12 only (EutHNPR), while the others were barely detectable in M9 glycerol $NH_4Cl$ and strongly upregulated in M9 glycerol EA B12, with fold changes ranging from 5 (EutJ) to 325 (EutM) (Fig.4A). This included enzymes linked to EA catabolism (EutAPQDEGBC) and the structural Eut BMC shell components (EutSMNLK). We calculated the abundance of each Eut protein in M9 glycerol EA B12 corrected for the number of theoretically observable tryptic peptides (iBAQ values[36]: Fig.4C), to correct for differences in molecular weight and amino-acid sequences. Relative to the most abundant protein, EutQ, an acetate kinase[37], whose relative abundance was set to 100, the most abundant predicted shell components were EutM, EutL, EutS, EutK and EutN with relative abundances of 96 ± 14, 39 ± 1, 11 ± 3, 8 ± 1, and 1 ± 1, respectively. The most abundant putative Eut BMC core enzymes besides EutQ were EutB, EutE, EutC, EutD, EutG and EutP (a second acetate kinase), with relative abundances of 37 ± 17, 27 ± 10, 24 ± 9, 10 ± 3, 7 ± 1 and 7 ± 1, respectively.

Eleven ancillary proteins are encoded within the EUT1 locus[4,16] (Fig.1A, Table S2). We could quantify 7 of them: the transketolase TktB, the transaldolase TalA, the malic enzyme MaeB, the N-acetylmuramoyl-L-alanine amidase AmiA, the putative acetyl-transferase YpeA, the protein of unknown function YfeY as well as the porphyrinogen oxidase YfeX (Table S4). None of these proteins were differentially accumulated in M9 glycerol EA B12 compared to M9 glycerol $NH_4Cl$. Distinct regulatory mechanisms therefore control their production as compared to the *eut* operon encoded elements, i.e. the presence of EA and vitamin B12 does not induce the accumulation of the ancillary proteins. The remaining ancillary EUT1 proteins were not detected, possibly because of low expression levels or a high hydrophobicity precluding their extraction/identification.

The second identified module consisted of proteins involved in maintaining intracellular N homeostasis (Fig.4B), a majority of which were more highly expressed in M9 glycerol EA B12, including the ammonium transporter AmtB, its cognate regulator GlnK and a two-component system (GlnG-GlnL) controlling N assimilation[38,39]. The second module also contained enzymes catalysing (de)amination reactions, such as asparagine synthetase (AsnAB), succinylglutamate semialdehyde dehydrogenase (AstCD), glutamine synthetase (GlnA), and guanine deaminase (GuaD). Proteins involved in the uptake of extracellular dipeptides (DdpAX), polypeptides (OppA) and amino acids (ArgT, CycA, HisQ) were also present. Several regulators and pathways normally mobilized under N starvation conditions were therefore activated in M9 glycerol EA B12, probably due to the absence of extracellular N sources other than EA. Note that the abundance of cobalamin-independent homocysteine transmethylase (MetE) was 7 times lower in M9 glycerol EA B12 than in M9 glycerol $NH_4Cl$. MetE normally participates in methionine biosynthesis but it can be replaced by MetH (cobalamin-dependent methionine synthase) in the presence of vitamin B12[40]

Overall, these results indicate that the production of Eut BMCs did not have a pleiotropic effect, since only proteins involved in BMC synthesis and N metabolism were affected.

*5) Analysis of EA utilization by exometabolomics.*

To decipher the metabolic functioning of the Eut BMCs, we grew W3110 WT under aerobic conditions in M9 derivatives containing glycerol as C source and either EA or $NH_4Cl$ as N source (Fig.S6A-B). Cyanocobalamin was again added to the EA-containing medium. The cultures reached similar maximal growth rates in both media (Table 3) but the biomass concentration after 12 h was higher with EA than with $NH_4Cl$ (0.97±0.01 $g_{DW}.L^{-1}$ VS 0.72±0.01 $g_{DW}.L^{-1}$).

The exometabolome was analysed by $^1$H-NMR and extracellular uptake and production fluxes were calculated from these data using PhysioFit[41] (Table 3; Fig.S6C-D). With $NH_4Cl$ as sole N source, glycerol was fully assimilated and no by-products were detected. With EA as sole N source, glycerol was

consumed at a similar rate and EA was assimilated at a rate of 7.8 ± 0.3 mmol.$g_{DW}^{-1}$.$h^{-1}$. Ethanol ($q_{P)EtOH}$ = 2.6 ± 0.1 mmol.$g_{DW}^{-1}$.$h^{-1}$) and acetate ($q_{P)Ace}$ = 1.7 ± 0.1 mmol.$g_{DW}^{-1}$.$h^{-1}$) were excreted, and the acetate was re-consumed upon exhaustion of glycerol and EA, explaining the higher final biomass under this condition. Trace amounts of acetaldehyde were also detected, suggesting that some acetaldehyde leaked from the Eut BMCs and escaped from the cells. Acetate, ethanol and acetaldehyde could all result from EA catabolism[20]. Assuming NADH is recycled within the Eut BMCs, acetate and EtOH should be produced in similar amounts[19]. Since the production rate of EtOH was significantly higher than that of acetate during exponential growth, this suggests either that some of the EA-derived acetate was used by cellular processes or that some of the EtOH was produced within the cytosol.

*6) Genome-scale predictions of EA utilization by E. coli.*

We next performed flux balance analysis (FBA[42]) on the same data to study the fate of EA in the Eut BMC and cytosol. We adapted the genome scale model (GSM) of *E. coli* iML1515[43] by compartmentalizing EA catabolism inside Eut BMCs, thereby ensuring that NADH and CoA-SH cofactors are recycled within the BMCs, while ATP is recycled in the cytosol (Fig.S7). The model was then constrained with the experimentally measured extracellular fluxes, assuming acetate and EtOH are produced in the BMCs. When maximizing biomass production, the maximal FBA-predicted growth rate was 0.72 $h^{-1}$. This value is higher than observed experimentally, indicating that glycerol and EA utilization are suboptimal *in vivo*. We therefore constrained the growth rate to the experimental value (Table 3: 0.45 $h^{-1}$) and defined ATP maintenance as the objective function[44] (Fig.S7). We also carried out flux variability analysis (FVA) to identify the optimal solution and the range of fluxes that each reaction can carry while maintaining at least 99 % of the objective.

The model predicted that Eut BMCs produce and release equimolar quantities of acetaldehyde, ethanol and acetyl-P into the cytosol, each accounting for 33 % of the C from EA (Fig.S7). Acetaldehyde can potentially escape from the cytosol into the extracellular medium, as reported previously[20], and/or be utilized in metabolism. All the ethanol is excreted. Some of the acetyl-P is converted into acetate (21 % of the C from EA) before excretion while the remaining portion can be converted into acetyl-CoA to fuel anabolism and thereby support growth (12 % of the C from EA) (Fig.S7). While EA is thought to act only as a nitrogen source for *E. coli* K-12, genome-scale modelling thus predicts that it may also provide carbon. Moreover, the model indicates that the amount of EA-derived ammonium exceeds the N needs of *E. coli* for growth, and a metabolic steady state can thus only be achieved if some of the ammonium (38 % of the N from EA) is excreted.

*7) $^{13}$C-metabolic flux analysis of EA and glycerol co-metabolism*

To test the predictions of the GSM, we performed a $^{13}$C-metabolic flux analysis of W3110 WT grown in M9 medium containing $^{12}C_3$-glycerol,$^{13}C_2$-EA as well as cyanocobalamin (Fig.5) and quantified the time-course concentrations of labelled and unlabelled EtOH and acetate by $^{1}$H-NMR (Fig.5A-B). EtOH was virtually fully labelled (4.66 ± 0.44 mM $^{13}C_2$-EtOH VS 0.47 ± 0.03 mM $^{12}C_2$-EtOH after 10 h, Fig.5B), demonstrating that about 90 % was produced from EA. The residual $^{12}C_2$-EtOH may have come either from incomplete encapsulation of Eut enzymes (e.g. EutE converting cysotolic $^{12}C_2$-acetyl-CoA into $^{12}C_2$-acetaldehyde and EutG, yielding $^{12}C_2$-EtOH), from cytosolic acetyl-CoA (produced from unlabelled glycerol) entering misassembled BMCs, or from weak cytosolic conversion of glycerol to ethanol through alternative cytosolic pathways. In contrast, only half of the acetate pool was labelled, indicating that EA and glycerol contributed equally to acetyl-P synthesis and thus to acetate production. The extracellular ammonium concentration, measured by $^{1}$H-NMR, increased from 0.4 ± 0.1 mM after 3 h to 4.4 ± 0.1 mM after 11 h (Fig.5B).

Finally, we built a dynamic isotopic model to quantify *in vivo* fluxes within and around the Eut BMCs by fitting the dynamics of all (labelled and unlabelled) exometabolites (Fig.5C; Table S5). This model includes a coarse-grained representation of glycolytic conversion of glycerol to acetyl-P and of the conversion of acetyl-P into acetate or its utilization elsewhere in metabolism for biomass synthesis, as suggested by the GSM. This model fit the data satisfactorily (Fig.S8), supporting the validity of the assumed network topology. Here, the Eut BMCs released more ethanol (Table S5; $v_{EutG}$ = 2.7 ± 0.1 mmol.$g_{DW}^{-1}$.$h^{-1}$, 37% of the C from EA) and acetyl-P ($v_{EutD}$ = 2.7 ± 0.1 mmol.$g_{DW}^{-1}$.$h^{-1}$, 37% of the C from EA) than acetaldehyde ($v_{BMC)acetaldehyde}$ = 1.7 ± 0.1 mmol.$g_{DW}^{-1}$.$h^{-1}$, 26% of the C from EA). Consistent with the labelling data, glycerol and EA contributed equally to the cytosolic acetyl-P pool (with $v_{Glycolysis}$ = 2.5 ± 0.1 mmol.$g_{DW}^{-1}$.$h^{-1}$). About 32 % of the acetyl-P pool was excreted as acetate ($q_{P)Acetate}$ = 1.6 ± 0.1 mmol.$g_{DW}^{-1}$.$h^{-1}$ ; 12% of the C from EA) and the rest fuelled growth ($v_{Pta}$ = 3.5 ± 0.1 mmol.$g_{DW}^{-1}$.$h^{-1}$ ; 25% of the C from EA). To confirm the significant anabolic utilization of carbon derived from EA, we measured the carbon isotopologue distributions of proteinogenic amino acids (Fig.5D). In keeping with the high $^{13}$C-enrichment of the cytosolic acetyl-P pool (and therefore also the acetyl-CoA pool) predicted by the isotopic model (Fig.S9), amino acids derived from the TCA cycle (i.e. Arg, Glu, Asp, Thr, Lys, Ile) had high fractions of heavy isotopologues. In contrast, amino acids produced from intermediates of the glycolytic and pentose phosphate pathways (i.e. Gly, Ser, His, Tyr, Phe, Ala, Val) had much lower $^{13}$C enrichment, pointing to an absence of neoglucogenic flux under the investigated conditions. Carbon derived from EA thus mainly entered central metabolism through the TCA cycle.

Regarding N metabolism, the isotopic model confirmed the ammonium overflow predicted by the GSM, with an ammonium production rate of 0.9 ± 0.2 mmol.$g_{DW}^{-1}$.$h^{-1}$ (Fig.5C; Table S5; 12% of the N from EA). This value is slightly lower than the optimal FBA-predicted value (3.0 mmol.$g_{DW}^{-1}$.$h^{-1}$, Fig.S7), possibly because of an underestimation of the quantity of N required to form biomass (which was determined during growth on glucose and ammonia as sole C and N sources, respectively[43]).

These isotope labelling experiments thus confirm the main predictions of the GSM, namely that EA can be used as a C source for growth and that N overflow occurs under these conditions.

## Discussion

The presence of functional Eut BMCs in *E. coli* has been suggested but never clearly demonstrated. Focusing on the non-pathogenic laboratory strain *E. coli* K-12, our interdisciplinary results provide deep molecular and functional insights into this native Eut BMC system and its importance for EA utilization.

We were able to visualize *E. coli* Eut BMCs *in cellula* by TEM and even more clearly by cryoET. The Eut BMCs produced by WT *E. coli* K-12 W3110 were mostly well formed with an electron-dense core separated from the surrounding cytoplasm by a continuous shell layer. Dark particles, presumably Eut enzymes, were present in the core. No array-like particle arrangements were observed, contrary to what has been reported for carboxysomes[45–49], but similar to observations of the Pdu BMCs of *Acetonema longum*[50]. While recent efforts have allowed the internal organisation of carboxysomes to be mapped out, much less is known of metabolosomes. Working on isolated Eut BMCs would facilitate downstream structural characterisation; however, our attempts to purify *E. coli* Eut BMCs using protocols established for Pdu BMCs[51] or α-carboxysomes[52] failed (data not shown). Apparently, the protein-protein interactions that allow Eut BMCs to assemble and/or persist *in vivo* do not withstand extracellular conditions[53]. Similar difficulties have previously been reported in *S. enterica*[51] and to our knowledge intact Eut BMCs have never been purified from any bacterial species so far, suggesting that Eut BMCs are intrinsically less stable than Pdu BMCs or carboxysomes.

We used fluorescence microscopy to observe Eut BMCs *in vivo*. $EutC_{(1-20)}$-GFP formed discrete puncta in M9 glycerol EA B12 only so upon *eut* induction, i.e. when all the other Eut components were present.

EutC$_{(1-20)}$-GFP was likely encapsulated inside the Eut BMC core under these conditions. Unlike fluorescently-tagged carboxysomes, which align along the cell axis[48], the EutC$_{(1-20)}$-GFP puncta moved freely around the cytoplasm. This sort of mobility has also been observed for SeEutC$_{1-19}$-EGFP encapsulated in *S. enterica* Eut BMCs *in vivo*[21,32]. Eut BMCs may interact with bacterial cytoskeleton through shell-coating proteins, somewhat like Pdu BMCs do with PduV[54]. EutP and PduV share some sequence homology (e.g. 28% primary structure identity and 54% similarity between EutP from *E. coli* K-12 and PduV from *S. enterica* LT2), both containing a RAS-like GTPase superfamily domain (Pfam10662). EutP may hence play a role in positioning the Eut BMCs, but this hypothesis remains to validate experimentally. How Eut BMCs subcellular dynamics affect their metabolic functioning or inheritance by daughter cells remains unclear. An EutK-mCherry fusion has recently been used to visualize *Listeria monocytogenes* Eut BMCs *in vivo*[55], which appeared as immobile red puncta. Future work should include the colocalization of core (e.g. EutC) and shell (e.g. EutK) elements to further validate the location of the fluorescent reporters.

How many Eut BMCs do the *E. coli* K-12 W3110 cells contain under our culturing conditions and how is the number of Eut BMCs regulated? Assuming that each GFP punctum corresponded to a single BMC, our data indicate that there were 6 Eut BMCs per bacterium, but this count needs to be confirmed by higher resolution approaches such as correlated light and electron microscopy[56]. In comparison, around 3-4 GFP puncta per bacterium were observed in *S. enterica* after labelling Pdu BMCs with GFP[57]. TEM observations indicate that chemo-autotrophic bacteria contain 3 to 80 carboxysomes per cell[34,48]. The number of Eut BMCs likely depends on culture conditions[9]: resource availability and specific regulatory networks (e.g. control by catabolic repression[10]) may modulate expression of the *eut* operon. Even with 5 to 100 BMCs per *E. coli* W3110 WT, Eut BMCs would occupy just 0.2-4 % of the total cytosolic volume.

This study also shows that the ability of *E. coli* K-12 to utilize EA as a N source hinges on the *eut* operon, with minor reorganizations of the rest of the proteome. However, expressing *eut* from even a low copy plasmid impaired growth. The underlying physiological cause is most likely the associated metabolic burden because slower growth i) also occurred in a medium containing $NH_4Cl$ as the N source (indicating that the impairment is not simply due to impaired EA catabolism) and ii) was more pronounced after inducing $P_{trc}$ with IPTG. Overexpressing the *eut* operon increased the number of Eut BMCs per bacterium observed by electron microscopy, up to several hundred under certain conditions (e.g. LB IPTG). The same effect (i.e. more Eut BMCs and slower growth) has previously been observed in *Enterococcus faecalis* upon suppressing a negative *eut* regulator[58]. As observed for other proteins[59,60], fine-tuned regulation of the *eut* operon is necessary to achieve the desired metabolic function at a manageable metabolic cost.

The protein complement of Eut BMCs remains unclear; however, our relative quantification of *E. coli* Eut proteins *in vivo* can be used to make an educated guess. The most abundant candidate shell component was hexameric (EutM), the second-most was trimeric (EutL) and the most dilute was pentameric (EutN), reminiscent of the Pdu BMC system in *S. enterica*[61]. This is consistent with EutM and EutL forming the facets and edges of the polyhedral shell together with other minor building blocks (i.e. EutS and EutK)[17,62]. As a pentameric vertex protein[17,63], EutN is less abundant than the other shell components. Among candidate core enzymes, the large (EutB) and small (EutC) subunits of EAL were roughly equimolar, consistent with the holoenzyme's predicted oligomeric state $[(EutB_2EutC_2)_3]$[64]. NADH generating EutE acetaldehyde dehydrogenase was another major putative core component as were Eut enzymes involved in cofactor recycling (EutG for $NAD^+$ and EutD for CoA-SH).

EutQ was found to be highly abundant, ten times more abundant than EutP, the other *eut*-encoded acetate kinase[37]. We think that EutQ and EutP are localized outside the Eut BMC (i.e. on the shell

surface or soluble in the cytosol) so that any ATP generated upon EA-derived acetyl-P consumption can feed into cellular metabolism. Moreover, EutP must be localized on the shell surface to interact with cytoskeleton elements. However, our results do not allow any conclusions to be drawn about the subcellular localizations of EutQ and EutP: either or both enzyme(s) could also be encapsulated within BMCs *in vivo*. EutQ has been reported to interact with EutM *in vitro* and to facilitate the formation of multiple Eut BMCs per bacterium[32]. Since ATP probably cannot transit through the pores in the shell[19], any ATP produced in the core by EutQ and EutP when converting acetyl-P into acetate would have to be recycled internally, e.g. to reactivate EAL after it undergoes catalytic inactivation[65,66]. During the finalization of the present manuscript, a study was released showing the cytosolic localization of EutP and the encapsulation of EutQ within Eut BMCs in *S. enterica* LT2 [67]. EutQ moreover seems to play a central role in connecting the Eut BMC core and shell elements[67].

To our knowledge, the flux map reported here is the first to connect the Eut BMC with central metabolism *in cellula*. Our results indicate that *E. coli* Eut BMCs leak non-negligible amounts of acetaldehyde (up to 33 % of the C from EA). In comparison, about 13 and 28 % of the C from 1,2-PD was found to be lost as propionaldehyde by the Pdu BMCs of *Salmonella enterica* [68] and *Propionobacter freudenreichii*[69], respectively. Leakage may thus be a common feature of metabolosomes. However, our cultures were performed under aerobic conditions with shaking, which favours gas exchanges and acetaldehyde evaporation[20]. These conditions are different from those encountered within the gut environment, where only limited quantities of oxygen diffuse through the mucosal surface to be consumed by facultative anaerobes such as *E. coli*[70]. Hence, less acetaldehyde losses may occur *in vivo* within the mammalian host. We did not observe any deleterious effect of acetaldehyde leakage on growth, suggesting that the concentration of acetaldehyde remained below the toxicity threshold in the cytosol[20]. In our model, the remaining acetaldehyde is converted inside the BMC core into equimolar quantities of ethanol and acetyl-P before diffusing out through shell pores. Some of the EA-derived C then enters central metabolism, mainly through the TCA cycle, to fuel growth. This result is in line with a recent report demonstrating that *E. coli* assimilates acetate (here derived from ethanolamine) with glycolytic substrates when the glycolytic flux is low, such as on glycerol[71], to feed anabolism. But why then is *E. coli* K-12 W3110 WT unable to grow with EA as sole C source? Perhaps the flux of EA assimilation simply did not meet cellular housekeeping demands. Additional comparisons with other *E. coli* strains, including some capable of utilizing EA as sole C source[10,12], are required to identify the underlying mechanisms.

Could some ancillary EUT1 proteins play a role in EA utilization? We detected 7 out of the 11 ancillary EUT1 proteins by proteomics (TktB, TalA, MaeB, AmiA, YpeA, YfeY and YfeX), none of them being differentially accumulated in M9 glycerol EA B12 VS M9 glycerol $NH_4Cl$. YpeA and YfeY have no known biological functions. AmiA participates in septum formation during cell division[72]. YfeX is a peroxidase that acts onto porphyrinogens to convert them into porphyrins [73]; *yfeX* is upregulated under anaerobic conditions and may participate in respiratory complexes recycling. The contributions of AmiA and YfeX to EA catabolism, if any, appears unclear. Under certain conditions, MaeB, TktB and TalA, on the other hand, may funnel some EA-derived C through gluconeogenesis and the pentose phosphate pathway. Malic enzyme activity plays an important metabolic role by connecting the TCA cycle with gluconeogenesis[74]. The *maeB* expression is moreover induced when *E. coli* grows on acetate[75]. MaeB may thus be key when *E. coli* grows using the EA-derived acetyl-P (or acetate) as its sole C source: after conversion into acetyl-CoA, these EA-derived compounds first enter central metabolism through the TCA cycle/glyoxylate shunt. MaeB would then direct some EA-derived C towards gluconeogenesis. TktB and TalA both participate in the pentose phosphate pathway (PPP)[76]. TktB and TalA would next direct some of the EA-derived C through the PPP, allowing the generation of multiple metabolites that are essential for biomass formation (erythrose-4P, ribulose-5P…). TalA, like other aldolases[77], may also be

able to condensate some EA-derived acetaldehyde (leaking from the Eut BMCs) with glyceraldehyde-3P to produce 1-deoxy-D-xylulose 5-phosphate (DXP), a precursor for the synthesis of vitamin B6. The ancillary EUT1 proteins may hence funnel some EA-derived C for the accumulation of biomass. However, in the present study, we had to perform our experiments in M9 glycerol EA B12 since *E. coli* K-12 W3110 does not grow on M9 EA B12 (i.e. with EA as the sole C/N source). In our medium, glycerol provides most C for both glycolysis and the pentose phosphate, as confirmed by the labelling patterns of proteinogenic amino-acids. The ancillary EUT1 proteins implication should therefore be re-assessed in *E. coli* strains that grow using EA as their C and N source, under more physiologically relevant conditions.

By integrating our microscopy and fluxomics data, we calculated the mean EA conversion flux through an individual *E. coli* K-12 Eut BMC *in cellula* (calculations in Supplementary Data 3): the value is close to 0.300 fmol.BMC$^{-1}$.h$^{-1}$ (or 0.600 fmol C.BMC$^{-1}$.h$^{-1}$). This is very close to the mean flux of 1,2-PD conversion through an individual *S. enterica* Pdu BMC *in cellula* (0.350 fmol.BMC$^{-1}$.h$^{-1}$, or 1.050 fmol C.BMC$^{-1}$.h$^{-1}$) calculated from previous experimental and modelling data[68,78]. The carboxylation rate through an individual carboxysome varies from 0.03 to 4.82 fmol C.BMC$^{-1}$.h$^{-1}$ depending on conditions[79]. These BMC types seem to operate at similar overall turnover rates, despite having different enzymatic core contents. Although they occupy an almost negligible fraction of the cytosolic volume, our model predicts that Eut BMCs act as efficient nanobioreactors with total C fluxes comparable to those of other major cellular metabolic processes (e.g. a glycolytic flux of 0.72 fmol.cell$^{-1}$.h$^{-1}$ or 2.16 fmolC.cell$^{-1}$.h$^{-1}$ here).

Finally, we also found that EA served as a N source, with strong modifications in the levels of proteins involved in nitrogen metabolism. The ammonium generated by EA catabolism was mostly used for biomass production but the rest was excreted. The N:C molar ratio of EA (1:2) is higher than in the elemental composition of *E. coli* (1:4)[80], which explains why our cultures acted as net ammonium producers. Moreover, given that glycerol was the primary C source in M9 glycerol EA B12, the proportion of excreted ammonium would likely be higher in other media with less organic C (e.g. M9 EA). Another study, released during the finalization of the present manuscript, showed that *E. coli* Nissle 1917 also displays an ammonium overflow when grown on M9 EA B12 while *S. enterica* does not[81]. This may have important physiological implications in the gut microbiome environment. Do EA-utilizing bacteria release ammonium in the gut, making it available for surrounding micro-organisms? EA utilization may influence the composition of complex bacterial communities through C and N overflows.

## Conclusion

The native *E. coli* Eut BMC has so far been overlooked by recent efforts to explore the natural diversity of BMC structures and functions. Our interdisciplinary approach shows that the laboratory strain *E. coli* K-12 W3110 produces well-formed Eut BMCs. These Eut BMCs act as orthogonal modules in the cytosol, turning EA into usable N and C substrates for biomass formation, but with significant metabolic overflow. However, some questions remain unanswered as to how the Eut BMCs operate, particularly regarding the subcellular localization of certain Eut proteins (e.g. EutQ) and of cofactor recycling (e.g. ATP). Several ancillary EUT1 proteins may be important for EA utilization but the hypothesis still awaits direct experimental validation. The existence of a native subcellular compartmentalization system shows that *E. coli* has a more complex metabolic organization than originally perceived.

## Materials and Methods

### Bacterial strains and culture conditions

*Media preparation*

Cloning experiments were performed in Lysogeny Broth (LB). For the physiological characterizations, a nitrogen-free M9-medium was first assembled containing (final concentration in the medium): 17.4 $g{\cdot}L^{-1}$ $Na_2HPO_4 \cdot 12H_2O$, 3.03 $g{\cdot}L^{-1}$ $KH_2PO4$, 0.51 $g{\cdot}L^{-1}$ NaCl, 0.49 $g{\cdot}L^{-1}$ MgSO4 and 4.38 $mg{\cdot}L^{-1}$ $CaCl_2$. Thiamine hydrochloride (100 $mg{\cdot}L^{-1}$) was also included, as well as 0.1 % (v/v) of a trace element solution (final concentration in the medium: 15 $mg{\cdot}L^{-1}$ $Na_2EDTA \cdot 2H_2O$,4.5 $mg{\cdot}L^{-1}$ $ZnSO_4 \cdot 7H_2O$, 0.3 $mg{\cdot}L^{-1}$ $CoCl_2 \cdot 6H_2O$, 1 $mg{\cdot}L^{-1}$ $MnCl_2 \cdot 4H_2O$, 1 mg $\cdot L^{-1}$ $H_3BO_3$, 0.4 $mg{\cdot}L^{-1}$ $Na_2MoO \cdot 2H_2O$, 3 $mg{\cdot}L^{-1}$ FeSO4 $\cdot 7H_2O$, and 0.3 $mg{\cdot}L^{-1}$ $CuSO_4 \cdot 5H_2O$). In M9 glycerol ammonium, $NH_4Cl$ (1.07 $g{\cdot}L^{-1}$ or 20 mM) was added as the nitrogen source and glycerol (2.76 $g{\cdot}L^{-1}$ or 30 mM) as the organic carbon source. In M9 glycerol EA B12, glycerol was the main organic carbon source (2.76 $g{\cdot}L^{-1}$ or 30 mM), ethanolamine was added as the nitrogen source (1.22 $g{\cdot}L^{-1}$ or 20 mM; from a stock solution at 122 $g{\cdot}L^{-1}$ adjusted to pH 7 with HCl 12 N) and cyanocobalamin was systematically included (200 nM). All media components were autoclaved except for thiamine hydrochloride, the trace element solution, $NH_4Cl$ and ethanolamine that were filter-sterilized instead (Minisart 0.2 mm syringe filter, Sartorius, Germany). Antibiotics were added to both solid and liquid media according to each strain's resistance profile [Ampicillin (Amp) at 100 $\mu g.mL^{-1}$, Kanamycin (Km) at 50 $\mu g.mL^{-1}$, Spectinomycin (Sp) at 50 $\mu g.mL^{-1}$ and/or Gentamycin (Gm) at 10 $\mu g.mL^{-1}$]. Isopropyl-b-D-thiogalactoside (IPTG) (final concentration 20 µM) or anhydrotetracycline (aTc) (final concentration 8ng $mL^{-1}$ or 80 ng $mL^{-1}$) was also incorporated when indicated. All chemical products were purchased from Sigma-Aldrich (France) unless otherwise specified.

*Strains cultivation*

*E. coli* K-12 W3110 wild-type (WT) as well as several mutant derivatives were used (Table 1). All the strains were cryopreserved at -80°C in LB with 25 % (w/v) glycerol. The strains were streaked onto LB agar plates and incubated at 37°C for 16 h. An isolated single colony then served to inoculate 2 ml of LB medium before culturing for 8h at 37°C under 200 rpm orbital shaking (Inova 4230, Brunswick Scientific, United States). The optical density at 600 nm ($OD_{600nm}$) was measured with a Genesys 6 spectrophotometer (Thermo Fisher Scientific, United States). The preculture was next diluted into a baffled shake flask (250 ml) containing 50 ml of modified M9-medium, aiming for a starting $OD_{600nm}$ of 0.07.

After 16h of incubation at 37°C under 200 rpm shaking, the bacteria were collected by centrifugation (4000 $\times$ g at room temperature for 3 min) and washed once using modified M9 medium. Finally, the bacteria were inoculated into a baffled flask (250 mL) containing 50 ml of modified M9 medium, again at a starting $OD_{600nm}$ of 0.07. Cultures were performed at 37°C under 200 rpm shaking to proceed with the physiological characterization. The following equation was employed to convert $OD_{600nm}$ values into corresponding biomass dry weight: $g_{DW} = 0.37 \times OD_{600nm}$.

When mentioned, cultures were made in a plate format instead. In this case, transparent flat-bottom 96 well plates (Sarstedt, Germany) covered with lids and containing 100 µl medium per well were used. The culturing scheme was similar to that described for shake flasks. A CLARIOStar Plus (BMG LabTech, Germany) plate reader apparatus allowed maintaining the cultures at 37°C under 200 rpm double orbital shaking. Absorbance at 600 nm was measured every 10 min to estimate growth. Results were analysed with the MARS Data Analysis software (BMG LabTech, Germany).

Molecular biology

*Cloning procedures*

Polymerase chain reactions (PCRs) for cloning purposes were performed using the high fidelity Phusion DNA Polymerase (NEB, France). PCR products were purified with the NucleoSpin PCR Clean Up kit (Macherey Nagel, Germany), quantified with a NanoDrop 2000 Spectrophotometer (Thermo Fisher Scientific, France) and assembled by In-Fusion (TaKaRa, Japan). After purification with the NucleoSpin Plasmid kit (Macherey Nagel, Germany), the generated plasmids were verified by Sanger Sequencing.

*CRISPR-Cas9 genome editing*

The system described by Jiang and coworkers was utilized in this study[27]. To generate the Δ*eut* strain, a pTargetF plasmid for *eutG* (pTargetF_eutG) was first constructed. The linear backbone from pTargetF was amplified with primers F_bb1/R_bb1 (see Table S1 for primer sequences). The *eutG* targeting protospacer (PAM shown in bold: CGGCACACCTTCGGTCAATG**CGG**) was amplified with primers F_eutGgRNA/R_eutGgRNA. The generated amplicons were then assembled by In-Fusion to generate pTarget_eutG ($Sp^R$). Next, the 500 nt situated directly upstream of the P*eut* promoter (upper homology arm) were amplified from purified *E. coli* K-12 W3110 WT gDNA with F_UA1/R_UA1. The same was achieved for the 500 nt downstream of *eutR* (lower homology arm) with F_LA1/R_LA1. The backbone from pUC19 was amplified with F_bb2/R_bb2 and all three fragments were assembled by In-Fusion to yield pHD_Δeut ($Amp^R$). The linear fragment containing both homology arms was amplified from pHD_Δeut using F_HD1/R_HD1. pTarget_eutG as well as the produced linear fragment were finally electroporated into pCas-containing *E. coli* K-12 W3110 WT bacteria to obtain chromosomally edited Δ*eut* strains. After genotyping, the edited mutants were cured of pTarget_eutG and pCas as described previously.

The *SS9* targeting protospacer (TCTGGCGCAGTTGATATGTA**AGG**) was cloned by In-Fusion into pTargetF using primers F_SS9gRNA/R_SS9gRNA and F_bb1/R_bb1, yielding pTargetF_SS9. The 1000 nt upstream of *SS9* were amplified from purified *E. coli* K-12 W3110 WT gDNA with F_UA2/R_UA2, including mutations to suppress the above-mentioned PAM (i.e. AGG to CAA), the 1000 nt downstream of *SS9* with F_LA2/R_LA2. The EutC-GFP and $EutC_{1\text{-}20}$-GFP encoding cassettes ($P_{LtetO\text{-}1}$ promoter, $T_{LT0}$ terminator) were synthesized and cloned with flanking the SS9 homology arms into pUC19, yielding pHD_SS9_eutC-GFP and pHD_SS9_$eutC_{1\text{-}20}$-GFP.

*Assembly of pEut_WT.*

The linear backbone from pSEVA661_Ptrc (modified version of pSEVA661 bearing a *lacI*$^q$ expression cassette and the $P_{trc}$ promoter cloned in its MCS) was amplified with primers F_bb3/R_bb3 (see Table S1). The complete *eut* operon was amplified from isolated *E. coli* K-12 W3110 WT gDNA using F_eut1/R_eut1, F_eut2/R_eut2 as well as F_eut3/R_eut3. The generated amplicons were assembled by In-Fusion to produce the low copy plasmid pEut_WT ($Gm^R$). Next generation DNA sequencing on an Ion S5 System (Thermo Fisher Scientific, France) was performed at the GeT_Biopuces platform (TBI, INSA Toulouse, France) to verify that the plasmid was properly assembled.

Microscopy observations

*Epifluorescence microscopy*

Samples (equivalent to 0.6 µl culture at $OD_{600nm}$ = 1) were collected after reaching stationary phase and deposited onto GeneFrames (ThermoFisher) containing solidified C-/N-free M9 medium with 1 % agarose. Phase contrast and fluorescence microscopy was performed at room temperature using an automated inverted epifluorescence microscope (Nikon Ti-E/B) equipped with the “perfect focus system” (PFS, Nikon), a phase contrast objective (Plan Apo 100x Oil Ph3 DM NA1.4), a Lumencor SpectraX Light Engine as the illumination source (Ex: 475/34 for GFP), Semrock Brightline multiband

dichroic filters (FF409/493/573/652-Di02 for GFP), Semrock emission filters (Em: 536BP40 for GFP) and a Flash4.0 sCMOS camera (Hamamatsu). Fluorescence images were captured and processed using Nis-Elements AR software (Nikon) as well as Fiji[82]. To visualize the mobile fluorescent puncta, pictures were taken every 5 sec over an interval of 30 sec. The puncta were counted manually within n = 30 bacterial cells per samples.

*TEM visualization*

Samples (equivalent to 1 ml of culture at $OD_{600nm}$ = 1) were collected upon reaching stationary phase by centrifugation at 3000 × g for 3 minutes. Pellets were resuspended in fixation solution (2.5 % glutaraldehyde, 0.1 M cacodylate pH 7.4 as well as 0,04 % w/v ruthenium red) and incubated for 16h at 4°C. Samples were post-fixated in 1 % osmium tetroxide, dehydrated stepwise in ethanol and eventually embedded in the Embed 812 resin (Electron Microscopy Sciences) with a Leica AMW automated device. Thin sections (70 nm width) were stained (solution containing 3 % uranyl acetate in 50 % ethanol as well as Reynold's lead citrate) and observed using a HT 7700 Hitachi transmission electron microscope (accelerating voltage 80 kV, CCD AMT XR41 camera).

*cryoET visualization*

Samples (equivalent to 1 ml of culture at $OD_{600nm}$ = 1) were collected upon reaching stationary phase and centrifuged at 3000 × g for 3 minutes. Supernatants were discarded. Pellets were washed twice in 1X PBS buffer pH 7.4 and finally resuspended in 50µl of 1X PBS 7.4.

Grid preparation: 3.4 µL of sample were deposited onto glow-discharged lacey carbon grids and placed in the thermostatic chamber of a Leica EM-GP automatic plunge freezer, set at 20°C and 95 % humidity. Excess solution was removed by blotting with Whatman n°1 filter paper for 2.5 seconds, and the grids were immediately flash frozen in liquid ethane at -185°C.

Cryo-electron tomography: Tilt-series were acquired on a Talos Arctica (Thermo Fisher Scientific) operated at 200 kV in parallel beam condition using either a K2 (for mutant cells) or K3 (for WT condition) Summit direct electron detector and a BioQuantum energy filter (Gatan Inc.) operated in zero-loss mode with a slit width of 20 eV. For WT cells, data collection was carried out using Tomo software (Thermo Fisher Scientific), at a nominal magnification of x31,000 with a calibrated pixel size of 2,78Å. For mutant cells, a nominal magnification of x49000 was used with a calibrated pixel size of 2.84Å. In both conditions, tilt series were acquired following the dose symmetric scheme[83] between +50° and −50° with a 2° tilt increment and a defocus range between -10 and -12 µm. Each tilt image was acquired in electron counting mode with cumulative electron dose of 140e-/$A^2$ fractionated into ten frames.

Tomogram reconstruction and segmentation: Movie frames were aligned using MotionCor2[84] and tilt series were mutually aligned by using 10nm gold particles as fiducial markers and the 3D volumes (tomograms) were reconstructed with weighted back projection using IMOD v.4.11.16[85] software packages with a binning factor of 4. Tomograms were finally denoised and contrast enhanced, boosting the signal to noise ratio (SNR), using Topaz[86] and nonlinear anisotropic diffusion filtering, respectively. Individual objects in tomograms are then segmented using EMAN2 TomoSeg[87], and surfaces of each segmented object are generated and visualized in ChimeraX[88].

Proteomics analysis

*E. coli* K-12 W3110 WT cultures were grown at 37°C under 200 rpm orbital shaking, in 250 ml flasks containing 50 ml M9 glycerol EA B12. Upon reaching $OD_{600nm}$ = 1, samples (40 ml) were collected and centrifuged 5 min at 4000 × g. Supernatant was discarded, pellet was resuspended in 3 ml Lysis Buffer

[100mM triethylammonium bicarbonate (TEAB) Buffer pH 8,5 with 2,5 % w/v SDS] at 4°C. Bacteria were lyzed by sonication (Fisherbrand sonicator equipped with a microprobe: 20 % power, 20 sec on, 30 sec off, cycle repeated twice). After centrifugation 8 min at 13000 × g, supernatant was collected. The protein concentration was determined using a BCA assay.

Dried protein extracts (40 µg) were solubilized with 25 µl of 5% SDS. Proteins were submitted to reduction and alkylation of cysteine residues by addition of TCEP and chloroacetamide to a final concentration respectively of 10 mM and 40 mM. Protein samples were then processed for trypsin digestion on S-trap Micro devices (Protifi) according to manufacturer's protocol, with the following modifications: precipitation was performed using 211 µl S-Trap buffer; 4 µg Trypsin was added per sample for digestion, in 25 µl TEAB 50mM pH8.

Tryptic peptides were resuspended in 20 µl of 2% acetonitrile and 0.05% trifluoroacetic acid and analyzed by nano-liquid chromatography (LC) coupled to tandem MS, using an UltiMate 3000 system (NCS-3500RS Nano/Cap System; Thermo Fisher Scientific) coupled to an Orbitrap QExactive Plus mass spectrometer (Thermo Fisher Scientific). 5 µl of each sample was loaded on a C18 precolumn (300 µm inner diameter × 5 mm, Thermo Fisher Scientific) in a solvent made of 2% acetonitrile and 0.05% trifluoroacetic acid, at a flow rate of 20 µl/min. After 5 min of desalting, the precolumn was switched online with the analytical C18 column (75 µm inner diameter × 50 cm, in-house packed with Reprosil C18) equilibrated in 95% solvent A (5% acetonitrile, 0.2% formic acid) and 5% solvent B (80% acetonitrile, 0.2% formic acid). Peptides were eluted using a 5%-50% gradient of solvent B over 115 min at a flow rate of 300 nl/min. The mass spectrometer was operated in data-dependent acquisition mode with the Xcalibur software. MS survey scans were acquired with a resolution of 70,000 and an AGC target of 3e6. The 10 most intense ions were selected for fragmentation by high-energy collision induced dissociation, and the resulting fragments were analyzed at a resolution of 17500, using an AGC target of 1e5 and a maximum fill time of 50 ms. Dynamic exclusion was used within 30 s to prevent repetitive selection of the same peptide.

Raw MS files were processed with the Mascot software (version 2.7.0) for database search and Proline[89] for label-free quantitative analysis (version 2.1.2). Data were searched against *Escherichia coli* entries of the UniProtKB protein database (release Swiss-Prot 2019_11_05, 23,135 entries). Carbamidomethylation of cysteines was set as a fixed modification, whereas oxidation of methionine was set as variable modifications. Specificity of trypsin/P digestion was set for cleavage after K or R, and two missed trypsin cleavage sites were allowed. The mass tolerance was set to 10 ppm for the precursor and to 20 mmu in tandem MS mode. Minimum peptide length was set to 7 amino acids, and identification results were further validated in Proline by the target decoy approach using a reverse database at both a PSM and protein false-discovery rate of 1%. For label-free relative quantification of the proteins across biological replicates and conditions, cross-assignment of peptide ions peaks was enabled inside group with a match time window of 1 min, after alignment of the runs with a tolerance of +/- 600 s.

The mass spectrometry proteomics data have been deposited to the ProteomeXchange Consortium via the PRIDE partner repository with the dataset identifier PXD048973.

Metabolomics analysis

*$^{1}$H-NMR analysis of culture supernatants*

*E. coli* K-12 W3110 WT cultures were grown at 37°C under 200 rpm orbital shaking, in 250 ml flasks containing 50 ml M9 glycerol NH4Cl or EA. For the labelling experiment, fully-labelled ethanolamine ($^{13}C_2$-ethanolamine, InnovaChem, France) was employed in the last culturing step for M9 glycerol EA

B12. Samples (500 µL) were collected every 60 min. Bacteria were immediately removed by filtration (Minisart 0.2 mm syringe filter, Sartorius, Germany) and the flow-through was kept at -20°C until further analysis. The flow-through was thawed and mixed (180 µL) with 20 µL of an internal standard containing 2.35 g/l deuterated trimethylsilylpropanoic acid (TSP-d4) solubilized in $D_2O$. The $^1$H-NMR analyses were performed using a quantitative zgpr30 sequence with water pre-saturation prior to acquisition on an Avance III 500-MHz spectrometer. The parameters were as follows: 286 K, 128K points, 4 dummy scans, 64 scans, interscan delay of 8.98 s. Three biological replicates were included for each medium. For the ammonium quantification experiment, the filtration flow through (690 µl, diluted 4X in MQ H2O) was mixed with 7.3 µl 4M $H_2SO_4$ and 2.7 µl MQ $H_2O$[90]. TSP-d4 dissolved in D2O (60 µl) was added to 540 µl of the mixture. A solvent suppression proton NMR sequence (zggpw5) at 286K with 32K points, 64 scans, 4 dummy scans, and an interscan delay of 10 s was then applied. Quantification was achieved through an external $NH_4Cl$ standard curve (200 mM, 8 mM, 2 mM, 0.5 mM and 0.1 mM $NH_4Cl$ diluted in M9 glycerol) analysed with $^1$H-NMR with the same acquisition parameters and the same sample preparation. Quantification of ammonium in solution was achieved by integration of NMR signals of protons (between 6.9 and 7.4 ppm) attached to nitrogen in an acidic medium, according to the different occurring species (i.e. $NH_4$, $NH_3D$, $NH_2D_2$,) in a mixture of $H_2O$ and $D_2O$ ($NHD_3$ and $ND_4$ in negligible amounts were not detected).

*Isotopic profiling of proteinogenic amino acids*

The same cultures as for NMR analyses were used. Biomass (500µl) was harvested at an $OD_{600nm}$ of 1 corresponding to mid-exponential phase. The biomass sample was immediately mixed with 3,5 ml pre-chilled (-20°C) quenching solution made of methanol-acetonitrile-$H_2O$ (4:4:2) containing 125 mM formic acid. The mixture was incubated at -20°C for at least 2 h and then centrifugated at 4500 × g 4°C for 5 min. The pellet was stored at -20°C until further usage. After thawing, the pellet was evaporated to dryness with an Orbitrap apparatus (Thermo Fisher Scientific, USA) and hydrolyzed for 16h at 105°C with 500 µL HCl 6N. Samples were washed twice before being resuspended into 250 µL ultrapure water and diluted (1:700) for the mass spectrometry analysis. LC-MS was performed on an Ultimate 3000 HPLC system (Dionex, CA, USA) coupled to an LTQ Orbitrap Velos mass spectrometer (Thermo Fisher Scientific, USA). Full scan HRMS analyses were performed in positive FTMS mode, the acquisition parameters and data analysis pipeline being identical to that previously described by Heuillet and coworkers[91]. IsoCor[92] allowed correcting for natural isotopic abundances to determine the carbon isotopologue distributions (CIDs).

Modelling

*Extracellular uptake and production fluxes*

Glycerol and ethanolamine uptake fluxes, acetate and ethanol production fluxes, and growth rates were calculated from glycerol, ethanolamine, acetate, ethanol, and biomass concentration−time profiles using PhysioFit (v1.0.1[41], https://github.com/MetaSys-LISBP/PhysioFit). Ethanol evaporation was considered when calculating ethanol production flux, as detailed in Peiro et al.[93] using an evaporation constant of 0.0379 $h^{-1}$ that was determined experimentally.

*Genome-scale modelling of glycerol and ethanolamine co-metabolism.*

The iML1515 *E. coli* genome scale model[43] was first updated by incorporating the EA assimilation reactions catalysed by Eut enzymes (EutBC, EutG, EutE, EutD as well as EutQ/P) and the Eut BMC subcellular compartment. We assumed that EutBC, EutG, EutE and EutD were all encapsulated within the Eut BMC core as suggested previously[20], while EutQ/P were assumed to be cytosolic. We also assumed cofactors (i.e. NAD(H) and CoA-SH) to not exchange between the eut BMC and the cytosol,

thus being recycled internally within the Eut BMC core. We finally assumed that acetate and ethanol originated from the Eut BMCs. Flux balance analyses and flux variability analyses were carried out using *cobrapy*[94] after constraining exchange fluxes with experimental uptake fluxes of *E. coli* K-12 W3110 WT (see results). The final model iDJ1518 and the scripts used to perform the calculations can be found at https://github.com/MetaSys-LISBP/ethanolamine_metabolism. The genome-scale model is also available from the BioModels database[95] (http://www.ebi.ac.uk/biomodels) with identifier MODEL2403010003.

*$^{13}$C-metabolic flux analysis.*

To quantify intracellular fluxes during growth of *E. coli* on glycerol and ethanolamine, we constructed a dynamic $^{13}$C-flux model following the approach detailed before[96] . The model contains 21 reactions, 20 species, and 3 compartments (the environment, the cytoplasm and the eut BMCs), and represents five processes: i) growth, ii) glycerol uptake and conversion into acetyl-phosphate (AcP) by glycolysis, iii) ethanolamine assimilation and conversion through the eut BMCs, iv) AcP utilization by the TCA cycle, v) acetate, acetaldehyde, ethanol and ammonia excretion (Figure 5).

The differential equations, which balance the concentrations of extracellular compounds (biomass, glycerol, ethanolamine, acetate and ethanol) and intracellular compounds (AcP, AcCoA, ethanolamine, ethanol, acetate, glycerol, NAD(H) and ammonia), were completed with isotopic equations for parameter estimation. As detailed before[97], we considered all reactions (except biomass synthesis) separately for unlabeled and labelled reactants. Fluxes were assumed to be constant over time since the cells were assumed to be at metabolic steady-state during exponential growth phase. We also took ethanol evaporation into account, which was modeled with a mass action rate law, using the evaporation constant determined experimentally in this study. The final model has 13 free parameters in total. These parameters ($p$) were estimated by fitting to the experimentally determined concentration dynamics of biomass, glycerol, ethanolamine, ethanol and unlabeled and labelled acetate, by minimizing the objective function f defined as the weighted sum of squared errors:

$f(p) = \sum_i \left(\frac{x_i - y_i(p)}{\sigma_i}\right)^2$ where $x_i$ is the experimental value of data point $i$, with an experimental standard deviation $\sigma_i$, and $y_i(p)$ is the corresponding simulated value. The objective function $f$ was minimised using the particle swarm optimisation algorithm (2,000 iterations with a swarm size of 50). The experimental and fitted data of one biological replicate are shown in Figure 5, and detailed results for all replicates are provided in Supplementary Figure 7 and Supplementary Data 2.

The model was constructed and analysed using COPASI[98] (v4.27) and is provided in SBML and COPASI formats in the Supplementary data 2 and at https://github.com/MetaSys-LISBP/ethanolamine_metabolism. The model has also been deposited in the Biomodels database (https://www.ebi.ac.uk/biomodels)[95] with the identifier MODEL2403010002 to ensure reproducibility and reusability. Extensive details on the model are provided in Supplementary Data 2.

*Calculation of the flux through individual BMCs*

All the detailed calculations are given in Supplementary Data 3.

**Acknowledgements:**

We thank Isabelle Fourquaux (CMEAB) and Sylvain Cantaloube (CBI-LITC) for their technical help. This work was funded by grants from INRAE (NANOBEs and ColiMATTERS projects) and by the ANR (FUNCEMM, ANR-23-CE44-0038). The work was also funded in part by grants from the Région Occitanie, European funds (Fonds Européens de Développement Régional, FEDER), Toulouse

Métropole, and the French Ministry of Research with the Investissement d'Avenir Infrastructures Nationales en Biologie et Santé program (ProFI, Proteomics French Infrastructure project, ANR-10-INBS-08). We acknowledge the METi imaging facility, member of the national infrastructure France-BioImaging supported by the French National Research Agency (ANR-10-INBS-04).

**Bibliography:**

1. Shively, J. M., Decker, G. L. & Greenawalt, J. W. Comparative ultrastructure of the thiobacilli. *J. Bacteriol.* **101**, 618–627 (1970).

2. Chen, P., Andersson, D. I. & Roth, J. R. The control region of the pdu/cob regulon in Salmonella typhimurium. *J. Bacteriol.* **176**, 5474–5482 (1994).

3. Kofoid, E., Rappleye, C., Stojiljkovic, I. & Roth, J. The 17-gene ethanolamine (eut) operon of Salmonella typhimurium encodes five homologues of carboxysome shell proteins. *J. Bacteriol.* **181**, 5317–5329 (1999).

4. Sutter, M., Melnicki, M. R., Schulz, F., Woyke, T. & Kerfeld, C. A. A catalog of the diversity and ubiquity of bacterial microcompartments. *Nat. Commun.* **12**, 1–12 (2021).

5. Stojiljkovic, I., Bäumler, A. J. & Heffron, F. Ethanolamine utilization in Salmonella typhimurium: nucleotide sequence, protein expression, and mutational analysis of the cchA cchB eutE eutJ eutG eutH gene cluster. *J. Bacteriol.* **177**, 1357–1366 (1995).

6. Bertin, Y. *et al.* Enterohaemorrhagic Escherichia coli gains a competitive advantage by using ethanolamine as a nitrogen source in the bovine intestinal content. *Environ. Microbiol.* **13**, 365–377 (2011).

7. Kaval, K. G. & Garsin, D. A. Ethanolamine utilization in bacteria. *MBio* **9**, (2018).

8. Zepeda-Rivera, M. *et al.* A distinct Fusobacterium nucleatum clade dominates the colorectal cancer niche. *Nature* **628**, 424–432 (2024).

9. Dadswell, K. *et al.* Bacterial microcompartment-mediated ethanolamine metabolism in Escherichia coli urinary tract infection. *Infect. Immun.* **87**, e00211-19 (2019).

10. Jones, P. W. & Turner, J. M. Interrelationships between the enzymes of ethanolamine metabolism in Escherichia coli. *Microbiology* **130**, 299–308 (1984).

11. Rowley, C. A., Anderson, C. J. & Kendall, M. M. Ethanolamine influences human commensal Escherichia coli growth, gene expression, and competition with enterohemorrhagic E. coli O157: H7. *MBio* **9**, e01429-18 (2018).

12. de Gouveia, M. I. M., Daniel, J., Garrivier, A., Bernalier-Donadille, A. & Jubelin, G. Diversity of ethanolamine utilization by human commensal Escherichia coli. *Res. Microbiol.* **174**, 103989 (2023).

13. Kendall, M. M., Gruber, C. C., Parker, C. T. & Sperandio, V. Ethanolamine controls expression of genes encoding components involved in interkingdom signaling and virulence in enterohemorrhagic Escherichia coli O157: H7. *MBio* **3**, e00050-12 (2012).

14. Tsoy, O., Ravcheev, D. & Mushegian, A. Comparative genomics of ethanolamine utilization. *J. Bacteriol.* **191**, 7157–7164 (2009).

15. Stewart, K. L., Stewart, A. M. & Bobik, T. A. Prokaryotic organelles: bacterial microcompartments in E. coli and Salmonella. *EcoSal Plus* **9**, (2020).

16. Axen, S. D., Erbilgin, O. & Kerfeld, C. A. A taxonomy of bacterial microcompartment loci constructed by a novel scoring method. *PLoS Comput Biol* **10**, e1003898 (2014).

17. Sutter, M., Greber, B., Aussignargues, C. & Kerfeld, C. A. Assembly principles and structure of a 6.5-MDa bacterial microcompartment shell. *Science (80-. ).* **356**, 1293–1297 (2017).

18. Tanaka, S., Sawaya, M. R. & Yeates, T. O. Structure and mechanisms of a protein-based organelle in Escherichia coli. *Science (80-. ).* **327**, 81–84 (2010).

19. Huseby, D. L. & Roth, J. R. Evidence that a metabolic microcompartment contains and recycles private cofactor pools. *J. Bacteriol.* **195**, 2864–2879 (2013).

20. Penrod, J. T. & Roth, J. R. Conserving a volatile metabolite: a role for carboxysome-like organelles in Salmonella enterica. *J. Bacteriol.* **188**, 2865–2874 (2006).

21. Choudhary, S., Quin, M. B., Sanders, M. A., Johnson, E. T. & Schmidt-Dannert, C. Engineered protein nano-compartments for targeted enzyme localization. *PLoS One* **7**, e33342 (2012).

22. Aussignargues, C., Paasch, B. C., Gonzalez-Esquer, R., Erbilgin, O. & Kerfeld, C. A. Bacterial microcompartment assembly: The key role of encapsulation peptides. *Commun. Integr. Biol.* **8**, e1039755 (2015).

23. Shively, J. M. *et al.* Sequence homologs of the carboxysomal polypeptide CsoS1 of the thiobacilli are present in cyanobacteria and enteric bacteria that form carboxysomes-polyhedral bodies. *Can. J. Bot.* **76**, 906–916 (1998).

24. Brinsmade, S. R., Paldon, T. & Escalante-Semerena, J. C. Minimal functions and physiological conditions required for growth of Salmonella enterica on ethanolamine in the absence of the metabolosome. *J. Bacteriol.* **187**, 8039–8046 (2005).

25. Chessher, A., Breitling, R. & Takano, E. Bacterial microcompartments: biomaterials for synthetic biology-based compartmentalization strategies. *ACS Biomater. Sci. Eng.* **1**, 345–351 (2015).

26. Held, M., Quin, M. B. & Schmidt-Dannert, C. Eut bacterial microcompartments: insights into their function, structure, and bioengineering applications. *Microb. Physiol.* **23**, 308–320 (2013).

27. Jiang, Y. *et al.* Multigene editing in the Escherichia coli genome via the CRISPR-Cas9 system. *Appl. Environ. Microbiol.* **81**, 2506–2514 (2015).

28. Amann, E., Ochs, B. & Abel, K.-J. Tightly regulated tac promoter vectors useful for the expression of unfused and fused proteins in Escherichia coli. *Gene* **69**, 301–315 (1988).

29. Silva-Rocha, R. *et al.* The Standard European Vector Architecture (SEVA): a coherent platform for the analysis and deployment of complex prokaryotic phenotypes. *Nucleic Acids Res.* **41**, D666–D675 (2013).

30. Bassalo, M. C. *et al.* Rapid and efficient one-step metabolic pathway integration in E. coli. *ACS Synth. Biol.* **5**, 561–568 (2016).

31. Lutz, R. & Bujard, H. Independent and tight regulation of transcriptional units in Escherichia coli via the LacR/O, the TetR/O and AraC/I1-I2 regulatory elements. *Nucleic Acids Res.* **25**, 1203–1210 (1997).

32. Held, M. *et al.* Engineering formation of multiple recombinant Eut protein nanocompartments in E. coli. *Sci. Rep.* **6**, 24359 (2016).

33. Lee, M. J., Palmer, D. J. & Warren, M. J. Biotechnological advances in bacterial

785 microcompartment technology. *Trends Biotechnol.* **37**, 325–336 (2019).

786 34. Iancu, C. V *et al.* Organization, structure, and assembly of α-carboxysomes determined by
787 electron cryotomography of intact cells. *J. Mol. Biol.* **396**, 105–117 (2010).

788 35. Szklarczyk, D. *et al.* STRING v11: protein–protein association networks with increased
789 coverage, supporting functional discovery in genome-wide experimental datasets. *Nucleic*
790 *Acids Res.* **47**, D607–D613 (2019).

791 36. Schwanhäusser, B. *et al.* Global quantification of mammalian gene expression control. *Nature*
792 **473**, 337–342 (2011).

793 37. Moore, T. C. & Escalante-Semerena, J. C. The EutQ and EutP proteins are novel acetate
794 kinases involved in ethanolamine catabolism: physiological implications for the function of the
795 ethanolamine metabolosome in S almonella enterica. *Mol. Microbiol.* **99**, 497–511 (2016).

796 38. Javelle, A., Severi, E., Thornton, J. & Merrick, M. Ammonium sensing in Escherichia coli: role of
797 the ammonium transporter AmtB and AmtB-GlnK complex formation. *J. Biol. Chem.* **279**,
798 8530–8538 (2004).

799 39. van Heeswijk, W. C., Westerhoff, H. V & Boogerd, F. C. Nitrogen assimilation in Escherichia
800 coli: putting molecular data into a systems perspective. *Microbiol. Mol. Biol. Rev.* **77**, 628–695
801 (2013).

802 40. Weissbach, H. & Brot, N. Regulation of methionine synthesis in Escherichia coli. *Mol.*
803 *Microbiol.* **5**, 1593–1597 (1991).

804 41. Le Gregam, L. *et al.* PhysioFit: a software to quantify cell growth parameters and extracellular
805 fluxes. *bioRxiv* 2010–2023 (2023).

806 42. Orth, J. D., Thiele, I. & Palsson, B. Ø. What is flux balance analysis? *Nat. Biotechnol.* **28**, 245–
807 248 (2010).

808 43. Monk, J. M. *et al.* i ML1515, a knowledgebase that computes Escherichia coli traits. *Nat.*
809 *Biotechnol.* **35**, 904–908 (2017).

810 44. Schuetz, R., Kuepfer, L. & Sauer, U. Systematic evaluation of objective functions for predicting
811 intracellular fluxes in Escherichia coli. *Mol. Syst. Biol.* **3**, 119 (2007).

812 45. Cameron, J. C., Wilson, S. C., Bernstein, S. L. & Kerfeld, C. A. Biogenesis of a bacterial
813 organelle: the carboxysome assembly pathway. *Cell* **155**, 1131–1140 (2013).

814 46. Faulkner, M. *et al.* Direct characterization of the native structure and mechanics of
815 cyanobacterial carboxysomes. *Nanoscale* **9**, 10662–10673 (2017).

816 47. Ni, T. *et al.* Structure and assembly of cargo Rubisco in two native α-carboxysomes. *Nat.*
817 *Commun.* **13**, 4299 (2022).

818 48. Savage, D. F., Afonso, B., Chen, A. H. & Silver, P. A. Spatially ordered dynamics of the bacterial
819 carbon fixation machinery. *Science (80-. ).* **327**, 1258–1261 (2010).

820 49. Evans, S. L. *et al.* Single-particle cryo-EM analysis of the shell architecture and internal
821 organization of an intact α-carboxysome. *Structure* **31**, 677–688 (2023).

822 50. Tocheva, E. I. *et al.* Structure and expression of propanediol utilization microcompartments in
823 Acetonema longum. *J. Bacteriol.* **196**, 1651–1658 (2014).

824 51. Sturms, R., Streauslin, N. A., Cheng, S. & Bobik, T. A. In Salmonella enterica, ethanolamine
825 utilization is repressed by 1, 2-propanediol to prevent detrimental mixing of components of

two different bacterial microcompartments. *J. Bacteriol.* **197**, 2412–2421 (2015).

52. Fang, Y. *et al.* Engineering and modulating functional cyanobacterial CO2-fixing organelles. *Front. Plant Sci.* **9**, 739 (2018).

53. Tsai, S. J. & Yeates, T. O. Bacterial microcompartments: insights into the structure, mechanism, and engineering applications. *Prog. Mol. Biol. Transl. Sci.* **103**, 1–20 (2011).

54. Parsons, J. B. *et al.* Synthesis of empty bacterial microcompartments, directed organelle protein incorporation, and evidence of filament-associated organelle movement. *Mol. Cell* **38**, 305–315 (2010).

55. Chatterjee, A., Kaval, K. G. & Garsin, D. A. Role of Ethanolamine Utilization and Bacterial Microcompartment Formation in Listeria monocytogenes Intracellular Infection. *bioRxiv* 2012–2023 (2023).

56. Hoffman, D. P. *et al.* Correlative three-dimensional super-resolution and block-face electron microscopy of whole vitreously frozen cells. *Science (80-. ).* **367**, eaaz5357 (2020).

57. Kennedy, N. W. *et al.* Linking the Salmonella enterica 1, 2-propanediol utilization bacterial microcompartment shell to the enzymatic core via the shell protein PduB. *J. Bacteriol.* **204**, e00576-21 (2022).

58. Kaval, K. G. *et al.* Ethanolamine utilization and bacterial microcompartment formation are subject to carbon catabolite repression. *J. Bacteriol.* **201**, e00703-18 (2019).

59. Glick, B. R. Metabolic load and heterologous gene expression. *Biotechnol. Adv.* **13**, 247–261 (1995).

60. Ceroni, F. *et al.* Burden-driven feedback control of gene expression. *Nat. Methods* **15**, 387–393 (2018).

61. Yang, M. *et al.* Decoding the stoichiometric composition and organisation of bacterial metabolosomes. *Nat. Commun.* **11**, 1976 (2020).

62. Kalnins, G. *et al.* Encapsulation mechanisms and structural studies of GRM2 bacterial microcompartment particles. *Nat. Commun.* **11**, 388 (2020).

63. Wheatley, N. M., Gidaniyan, S. D., Liu, Y., Cascio, D. & Yeates, T. O. Bacterial microcompartment shells of diverse functional types possess pentameric vertex proteins. *Protein Sci.* **22**, 660–665 (2013).

64. Shibata, N. *et al.* Crystal structures of ethanolamine ammonia-lyase complexed with coenzyme B12 analogs and substrates. *J. Biol. Chem.* **285**, 26484–26493 (2010).

65. Mori, K., Bando, R., Hieda, N. & Toraya, T. Identification of a reactivating factor for adenosylcobalamin-dependent ethanolamine ammonia lyase. *J. Bacteriol.* **186**, 6845–6854 (2004).

66. Costa, F. G. & Escalante-Semerena, J. C. Localization and interaction studies of the Salmonella enterica ethanolamine ammonia-lyase (EutBC), its reactivase (EutA), and the EutT corrinoid adenosyltransferase. *Mol. Microbiol.* **118**, 191–207 (2022).

67. Yang, M. *et al.* Molecular basis of the biogenesis of a protein organelle for ethanolamine utilization. *bioRxiv* 2005–2024 (2024).

68. Sampson, E. M. & Bobik, T. A. Microcompartments for B12-dependent 1, 2-propanediol degradation provide protection from DNA and cellular damage by a reactive metabolic intermediate. *J. Bacteriol.* **190**, 2966–2971 (2008).

69. Dank, A. *et al.* Bacterial microcompartment-dependent 1, 2-propanediol utilization of Propionibacterium freudenreichii. *Front. Microbiol.* **12**, 679827 (2021).

70. Moreira de Gouveia, M. I., Bernalier-Donadille, A. & Jubelin, G. Enterobacteriaceae in the Human Gut: Dynamics and Ecological Roles in Health and Disease. *Biology (Basel).* **13**, 142 (2024).

71. Millard, P., Gosselin-Monplaisir, T., Uttenweiler-Joseph, S. & Enjalbert, B. Acetate is a beneficial nutrient for E. coli at low glycolytic flux. *EMBO J.* e113079 (2023).

72. Heidrich, C. *et al.* Involvement of N-acetylmuramyl-L-alanine amidases in cell separation and antibiotic-induced autolysis of Escherichia coli. *Mol. Microbiol.* **41**, 167–178 (2001).

73. Dailey, H. A. *et al.* The Escherichia coli protein YfeX functions as a porphyrinogen oxidase, not a heme dechelatase. *MBio* **2**, 10–1128 (2011).

74. Bologna, F. P., Andreo, C. S. & Drincovich, M. F. Escherichia coli malic enzymes: two isoforms with substantial differences in kinetic properties, metabolic regulation, and structure. *J. Bacteriol.* **189**, 5937–5946 (2007).

75. Oh, M.-K., Rohlin, L., Kao, K. C. & Liao, J. C. Global expression profiling of acetate-grown Escherichia coli∗. *J. Biol. Chem.* **277**, 13175–13183 (2002).

76. Rahman, M. & Shimizu, K. Altered acetate metabolism and biomass production in several Escherichia coli mutants lacking rpoS-dependent metabolic pathway genes. *Mol. Biosyst.* **4**, 160–169 (2008).

77. Schürmann, M., Schürmann, M. & Sprenger, G. A. Fructose 6-phosphate aldolase and 1-deoxy-D-xylulose 5-phosphate synthase from Escherichia coli as tools in enzymatic synthesis of 1-deoxysugars. *J. Mol. Catal. B Enzym.* **19**, 247–252 (2002).

78. Jakobson, C. M., Tullman-Ercek, D., Slininger, M. F. & Mangan, N. M. A systems-level model reveals that 1, 2-Propanediol utilization microcompartments enhance pathway flux through intermediate sequestration. *PLoS Comput. Biol.* **13**, e1005525 (2017).

79. Mangan, N. M. & Brenner, M. P. Systems analysis of the CO2 concentrating mechanism in cyanobacteria. *Elife* **3**, e02043 (2014).

80. Heldal, M., Norland, S. & Tumyr, O. X-ray microanalytic method for measurement of dry matter and elemental content of individual bacteria. *Appl. Environ. Microbiol.* **50**, 1251–1257 (1985).

81. Clare, C., Rutter, J. W., Fedorec, A. J. H., Frank, S. & Barnes, C. P. Bacterial microcompartment utilisation in the human commensal Escherichia coli Nissle 1917. *bioRxiv* 2005–2024 (2024).

82. Schindelin, J. *et al.* Fiji: an open-source platform for biological-image analysis. *Nat. Methods* **9**, 676–682 (2012).

83. Hagen, W. J. H., Wan, W. & Briggs, J. A. G. Implementation of a cryo-electron tomography tilt-scheme optimized for high resolution subtomogram averaging. *J. Struct. Biol.* **197**, 191–198 (2017).

84. Mastronarde, D. N. Automated electron microscope tomography using robust prediction of specimen movements. *J. Struct. Biol.* **152**, 36–51 (2005).

85. Kremer, J. R., Mastronarde, D. N. & McIntosh, J. R. Computer visualization of three-dimensional image data using IMOD. *J. Struct. Biol.* **116**, 71–76 (1996).

86. Bepler, T., Kelley, K., Noble, A. J. & Berger, B. Topaz-Denoise: general deep denoising models

for cryoEM and cryoET. *Nat. Commun.* **11**, 5208 (2020).

87. Chen, M. *et al.* A complete data processing workflow for cryo-ET and subtomogram averaging. *Nat. Methods* **16**, 1161–1168 (2019).

88. Pettersen, E. F. *et al.* UCSF ChimeraX: Structure visualization for researchers, educators, and developers. *Protein Sci.* **30**, 70–82 (2021).

89. Bouyssié, D. *et al.* Proline: an efficient and user-friendly software suite for large-scale proteomics. *Bioinformatics* **36**, 3148–3155 (2020).

90. Hodgetts, R. Y. *et al.* Refining universal procedures for ammonium quantification via rapid 1H NMR analysis for dinitrogen reduction studies. *ACS Energy Lett.* **5**, 736–741 (2020).

91. Heuillet, M. *et al.* Methodology for the validation of isotopic analyses by mass spectrometry in stable-isotope labeling experiments. *Anal. Chem.* **90**, 1852–1860 (2018).

92. Millard, P., Letisse, F., Sokol, S. & Portais, J.-C. IsoCor: correcting MS data in isotope labeling experiments. *Bioinformatics* **28**, 1294–1296 (2012).

93. Peiro, C. *et al.* Chemical and metabolic controls on dihydroxyacetone metabolism lead to suboptimal growth of Escherichia coli. *Appl. Environ. Microbiol.* **85**, e00768-19 (2019).

94. Ebrahim, A., Lerman, J. A., Palsson, B. O. & Hyduke, D. R. COBRApy: constraints-based reconstruction and analysis for python. *BMC Syst. Biol.* **7**, 1–6 (2013).

95. Malik-Sheriff, R. S. *et al.* BioModels—15 years of sharing computational models in life science. *Nucleic Acids Res.* **48**, D407–D415 (2020).

96. Millard, P., Enjalbert, B., Uttenweiler-Joseph, S., Portais, J.-C. & Létisse, F. Control and regulation of acetate overflow in Escherichia coli. *Elife* **10**, e63661 (2021).

97. Millard, P., Portais, J.-C. & Mendes, P. Impact of kinetic isotope effects in isotopic studies of metabolic systems. *BMC Syst. Biol.* **9**, 1–13 (2015).

98. Hoops, S. *et al.* COPASI—a complex pathway simulator. *Bioinformatics* **22**, 3067–3074 (2006).

**Figure legends:**

**Table 1. Bacterial strains and plasmids used in the study.**

**Table 2. Growth of *E. coli* K-12 W3110 strains grown in various M9 medium derivatives.** These experiments were performed using a microplate reader. Data are shown as mean (n = 3 biological replicates) ± standard deviation.

**Table 3. Growth parameters of *E. coli* K12 W3110 WT grown aerobically in M9 medium containing glycerol as C source and $NH_4Cl$ or EA as N source.** The exponential growth rate μ is expressed in $h^{-1}$; the substrate uptake ($q_S$) and product formation ($q_P$) rates are expressed in $mmol.(gDW.h)^{-1}$. DW: dry weight; ND: not detected. Data are shown as mean (n = 3 biological replicates) ± standard deviation.

**Figure 1. The *eut* operon is essential for EA utilization as nitrogen source by *E. coli* K-12 W3110.** A) Schematic representation of the chromosomal EUT1 locus in W3110 WT. Genes in grey flank the *eut* operon and are conserved amongst the EUT1 loci of Beta- and Gammaproteobacteria. Genes with other colours form the *eut* operon. Genes colored in yellow encode structural components of the Eut BMC shell, those in blue code for enzymes (EA catabolism, coenzyme B12 biosynthesis) and those in white encode other functions (chaperon, transporter). B) to E) Plate reader measurements of optical density at 600 nm for strains grown in B) M9 medium containing glycerol (30 mM) as C source and

$NH_4Cl$ (20 mM) as N source; C) M9 medium containing glycerol (30 mM) as C source and EA (20 mM) as N source, including vitamin B12 (200 nM); D) M9 glycerol $NH_4Cl$ with IPTG (20 µM) and E) M9 glycerol EA vitamin B12 with IPTG (20 µM). All the strains and plasmids are described in Table 1. Gentamicin (10 $\mu g.mL^{-1}$) was added for the plasmid-bearing strains. The data shown are from a representative experiment of at least three independent replicates.

**Figure 2. The chimeric protein EutC-GFP forms disctinct puncta in EA-containing medium.** A) Schematic representation of the $P_{LtetO-1}$::*eutC-GFP* expression cassette. This construct was inserted at the *SS9* safe chromosomal locus in W3110 WT to produce W3110 *eutC-GFP*. B), C) and D) Representative micrographs showing phase contrast images, GFP fluorescence signals, and composite images from W3110 *eutC-GFP* grown in B) M9 glycerol $NH_4Cl$ with 8 $ng.ml^{-1}$ aTc, C) M9 glycerol EA vitamin B12 with 8 $ng.ml^{-1}$ aTc and D) M9 glycerol EA vitamin B12 with 80 $ng.ml^{-1}$ aTc. Scale bars indicate 2 µm. E) Box plots indicating the number of GFP puncta per bacterium (n = 30 analyzed cells) for cultures grown in M9 glycerol EA vitamin B12 with 8 $ng.ml^{-1}$ or 80 $ng.ml^{-1}$ aTc.

**Figure 3. *E. coli* K-12 W3110 produces well-formed Eut BMCs.** A) Representative electron cryotomogram slice of W3110 WT grown in M9 glycerol EA vitamin B12 and B) Associated 3D segmentation showing the cellular membranes in grey, the ribosomes in green, and the Eut BMCs in blue. C) and D) Expanded views of Eut BMCs illustrating their variety in size and shape. The yellow arrows in D) point towards possible cryoET (missing wedge) artefacts or partially assembled BMCs . E) Representative tomogram slice of W3110 Δeut pEut_WT grown in M9 glycerol EA IPTG and F) Associated segmentation. Scale bars indicate 100 nm.

**Figure 4. EA utilization requires minimal reorganization of the proteome.** Cultures were grown aerobically in M9 glycerol EA vitamin B12 VS M9 glycerol $NH_4Cl$. Samples were collected for label-free quantitative mass spectrometry-based proteomics analyses. A) Volcano plot with Eut proteins (fold change > 2, $p < 0.05$) as red triangles, other upregulated proteins (fold change > 2, $p < 0.05$) as orange squares, downregulated proteins (fold change < -2, $p < 0.05$) as blue triangles, and unaffected proteins as black circles. B) Protein-protein interaction network as determined using STRING v11.5. Only selected upregulated (white outline) and downregulated (black outline) proteins are shown. Thicker lines indicate greater confidence in the considered protein-protein interactions. C) Normalized abundance (IBAQ score) of Eut proteins in M9 glycerol EA vitamin B12, using EutQ as the reference. Data shown are the mean of n = 4 biological replicates, bars correspond to standard deviations.

**Figure 5. The *E. coli* K12 W3110 Eut BMCs turn EA into usable C and N sources.** W3110 WT was grown aerobically in M9 medium containing $^{12}C_3$-glycerol and $^{13}C_2$-EA. A) Biomass accumulation (grams dry weight, gDW) and substrate consumption (mM); B) Product excretion. The substrates and products were quantified by $^1$H-NMR. Data shown are the average of n = 3 biological replicates, bars correspond to standard deviations. C) Experimental and predicted fluxes through EA and glycerol metabolisms using an isotopic model. Absolute flux values are summarized in Table S4. Blue-filled circles indicate metabolites and green-filled rectangles indicate proteins. Unidentified sinks are indicated as barred white circles. D) Carbon isotopologue distribution (CID) within proteinogenic aminoacids from biomass samples harvested during exponential growth, showing the intracellular incorporation of $^{13}C$ derived from EA. AAL: acetaldehyde; AcCoA: acetyl-CoA; Ace: acetate; AcP: acetyl-phosphate; EtOH: ethanol; $NH_4$: ammonium.

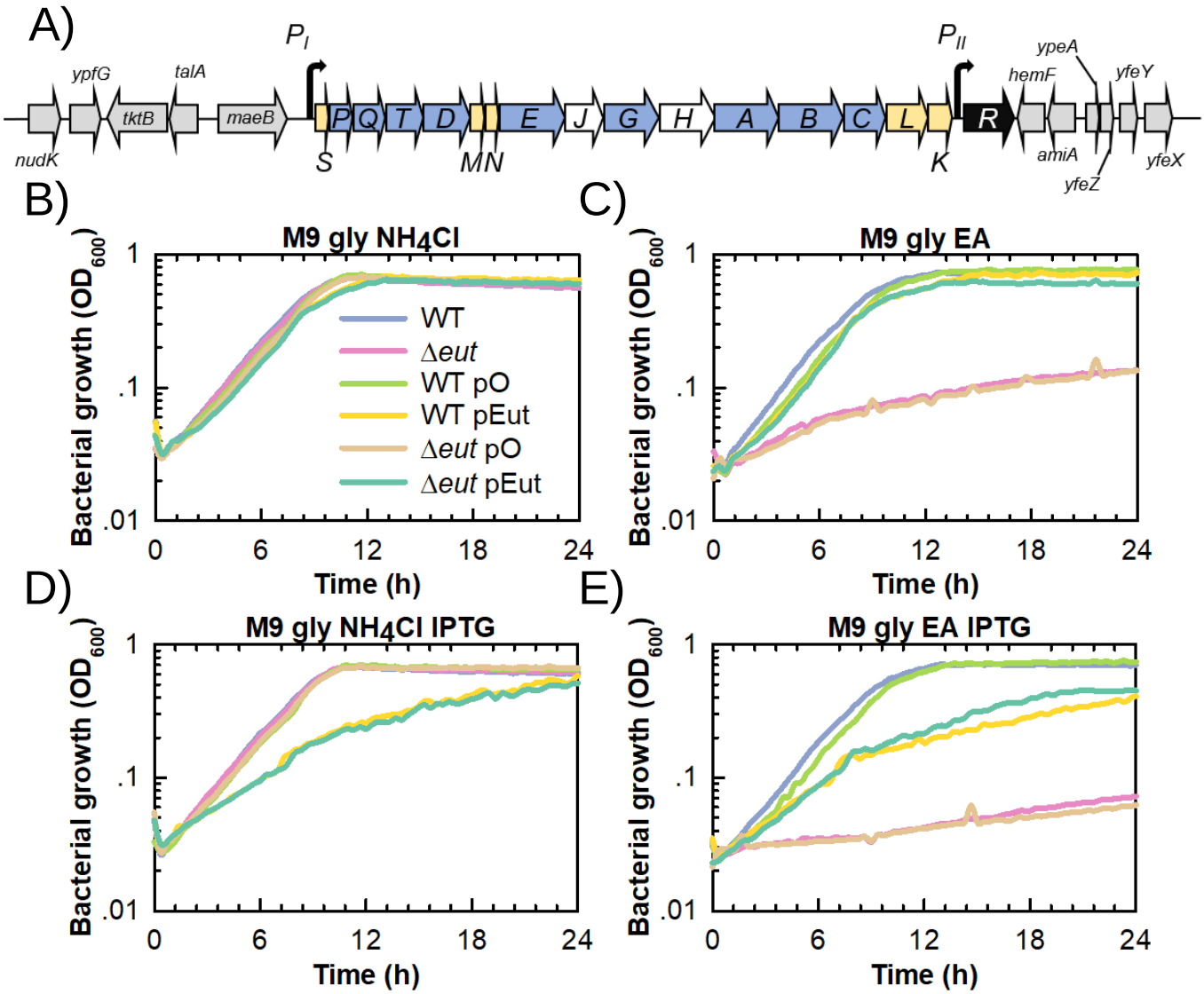


**Figure 1. The *eut* operon is essential for EA utilization as nitrogen source by *E. coli* K-12 W3110.** A) Schematic representation of the chromosomal EUT1 locus in W3110 WT. Genes in grey flank the *eut* operon and are conserved amongst the EUT1 loci of Beta- and Gammaproteobacteria. Genes with other colours form the *eut* operon. Genes colored in yellow encode structural components of the Eut BMC shell, those in blue code for enzymes (EA catabolism, coenzyme B12 biosynthesis) and those in white encode other functions (chaperon, transporter). B) to E) Plate reader measurements of optical density at 600 nm for strains grown in B) M9 medium containing glycerol (30 mM) as C source and $NH_4Cl$ (20 mM) as N source; C) M9 medium containing glycerol (30 mM) as C source and EA (20 mM) as N source, including vitamin B12 (200 nM); D) M9 glycerol $NH_4Cl$ with IPTG (20 µM) and E) M9 glycerol EA vitamin B12 with IPTG (20 µM). All the strains and plasmids are described in Table 1. Gentamicin (10 µg.mL$^{-1}$) was added for the plasmid-bearing strains. The data shown are from a representative experiment of at least three independent replicates.

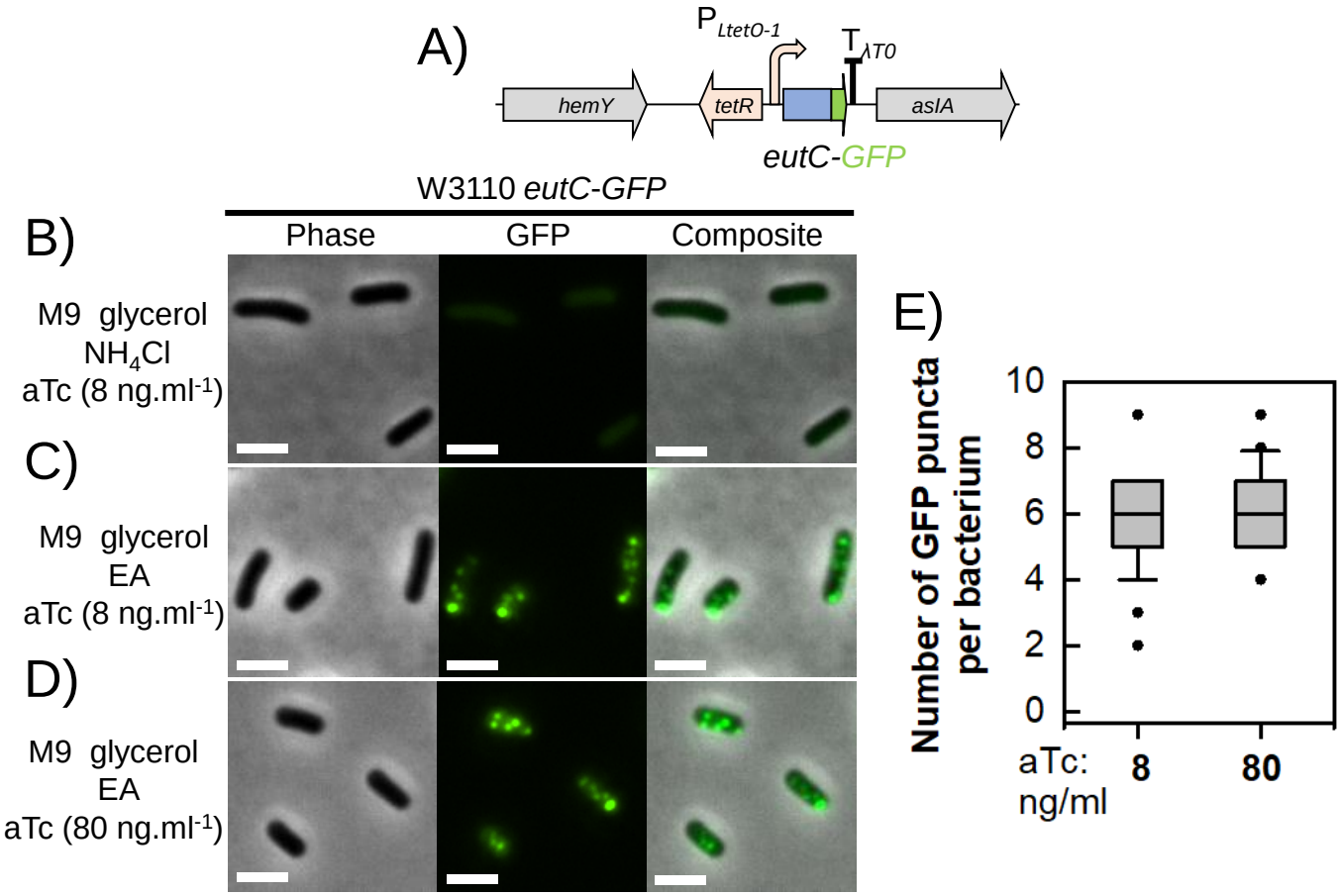


**Figure 2. The chimeric protein EutC-GFP forms disctinct puncta in EA-containing medium.** A) Schematic representation of the $P_{LtetO-1}$::*eutC-GFP* expression cassette. This construct was inserted at the *SS9* safe chromosomal locus in W3110 WT to produce W3110 *eutC-GFP*. B), C) and D) Representative micrographs showing phase contrast images, GFP fluorescence signals, and composite images from W3110 *eutC-GFP* grown in B) M9 glycerol $NH_4Cl$ with 8 ng.ml$^{-1}$ aTc, C) M9 glycerol EA vitamin B12 with 8 ng.ml$^{-1}$ aTc and D) M9 glycerol EA vitamin B12 with 80 ng.ml$^{-1}$ aTc. Scale bars indicate 2 µm. E) Box plots indicating the number of GFP puncta per bacterium (n = 30 analyzed cells) for cultures grown in M9 glycerol EA vitamin B12 with 8 ng.ml$^{-1}$ or 80 ng.ml$^{-1}$ aTc.

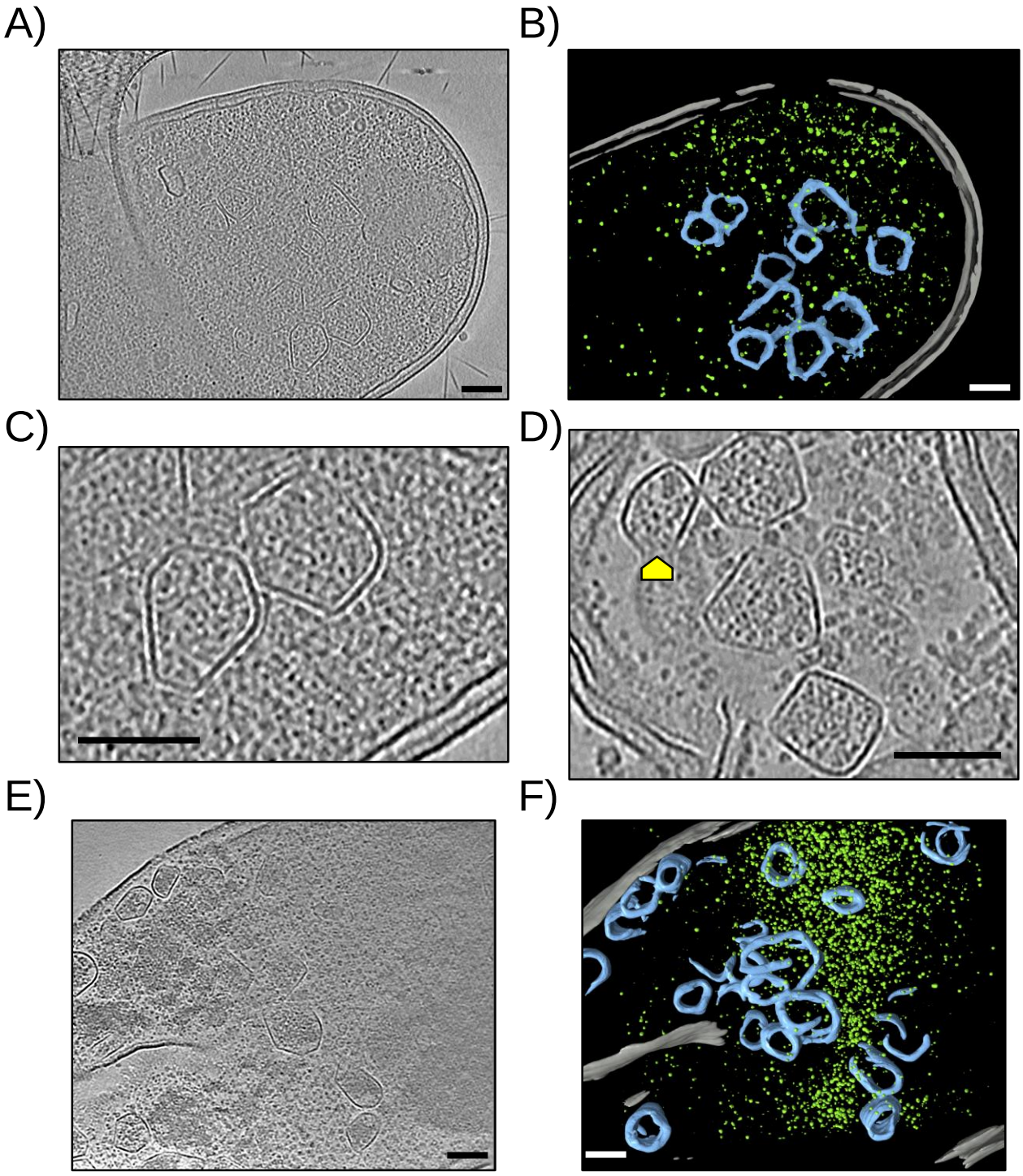


**Figure 3. *E. coli* K-12 W3110 produces well-formed Eut BMCs.** A) Representative electron cryotomogram slice of W3110 WT grown in M9 glycerol EA vitamin B12 and B) Associated 3D segmentation showing the cellular membranes in grey, the ribosomes in green, and the Eut BMCs in blue. C) and D) Expanded views of Eut BMCs illustrating their variety in size and shape. The yellow arrows in D) point towards possible cryoET (missing wedge) artefacts or partially assembled BMCs . E) Representative tomogram slice of W3110 Δeut pEut_WT grown in M9 glycerol EA IPTG and F) Associated segmentation. Scale bars indicate 100 nm.

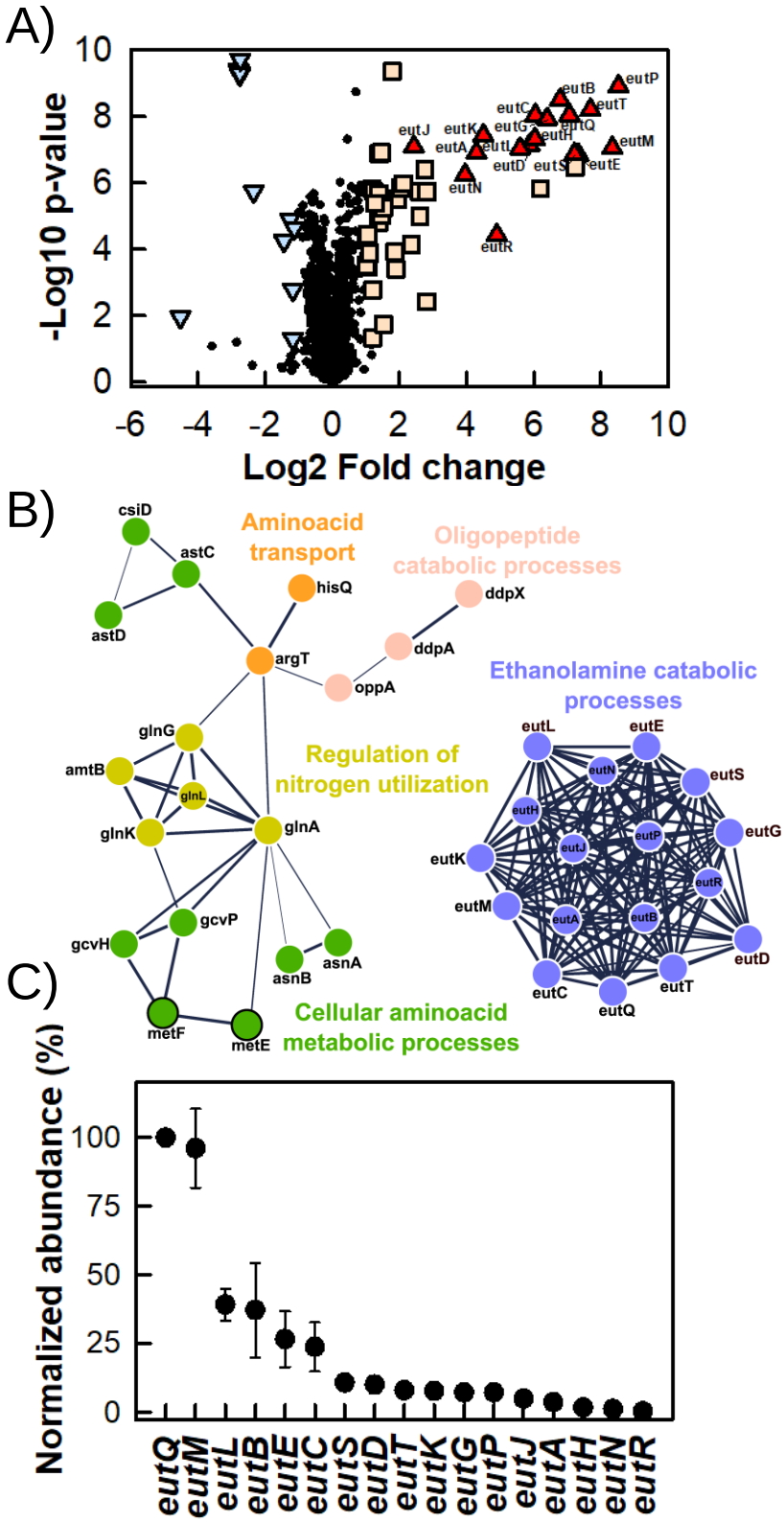


**Figure 4. EA utilization requires minimal reorganization of the proteome.** Cultures were grown aerobically in M9 glycerol EA vitamin B12 VS M9 glycerol $NH_4Cl$. Samples were collected for label-free quantitative mass spectrometry-based proteomics analyses. A) Volcano plot with Eut proteins (fold change > 2, $p < 0.05$) as red triangles, other upregulated proteins (fold change > 2, $p < 0.05$) as orange squares, downregulated proteins (fold change < -2, $p < 0.05$) as blue triangles, and unaffected proteins as black circles. B) Protein-protein interaction network as determined using STRING v11.5. Only selected upregulated (white outline) and downregulated (black outline) proteins are shown. Thicker lines indicate greater confidence in the considered protein-protein interactions. C) Normalized abundance (IBAQ score) of Eut proteins in M9 glycerol EA vitamin B12, using EutQ as the reference. Data shown are the mean of n = 4 biological replicates, bars correspond to standard deviations.

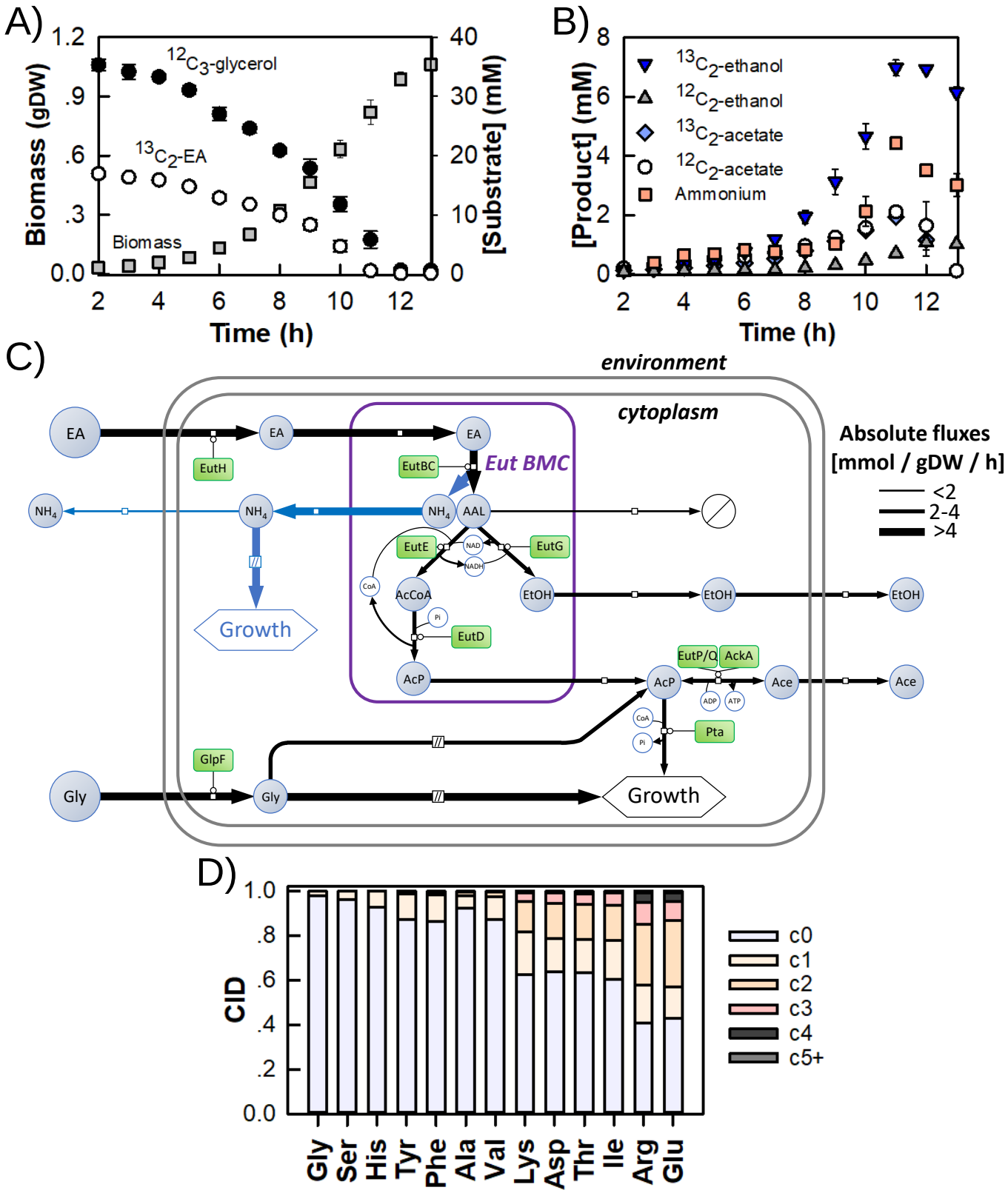


**Figure 5. The *E. coli* K12 W3110 Eut BMCs turn EA into usable C and N sources.** W3110 WT was grown aerobically in M9 medium containing $^{12}C_3$-glycerol and $^{13}C_2$-EA. A) Biomass accumulation (grams dry weight, gDW) and substrate consumption (mM); B) Product excretion. The substrates and products were quantified by $^{1}$H-NMR. Data shown are the average of n = 3 biological replicates, bars correspond to standard deviations. C) Experimental and predicted fluxes through EA and glycerol metabolisms using an isotopic model. Absolute flux values are summarized in Table S4. Blue-filled circles indicate metabolites and green-filled rectangles indicate proteins. Unidentified sinks are indicated as barred white circles. D) Carbon isotopologue distribution (CID) within proteinogenic aminoacids from biomass samples harvested during exponential growth, showing the intracellular incorporation of $^{13}$C derived from EA. AAL: acetaldehyde; AcCoA: acetyl-CoA; Ace: acetate; AcP: acetyl-phosphate; EtOH: ethanol; $NH_4$: ammonium.

| Strains or plasmids | Genotype or description | Source |
|---|---|---|
| ***E. coli* bacterial strains** | | |
| W3110 WT | *E. coli* K-12 W3110 wild-type [$F^-$ $\lambda^-$ INV(*rrnD-rrnE*) *rph-1* $eut^+$] | Laboratory collection |
| BW25113 WT | *E. coli* K-12 W3110 wild-type [$F^-$ $\lambda^-$ Δ*lacZ4787*(::*rrnB-3*) *hsdR514* Δ*(araBAD)567* Δ*(rhaBAD)568 rph-1* $eut^-$(*:: cryptic prophage DNA*)] | Laboratory collection |
| W3110 Δ*eut* | Chromosomal *eut* operon removed by genome editing in W3110 WT | This study |
| BW25113 *eut*+ | Cryptic prophage DNA insertion within the chromosomal *eut* operon removed by genome editing in BW25113 WT | This study |
| W3110 *eutC-GFP* | $P_{LtetO-1}$::*eutC-GFP* construct inserted at the SS9 safe chromosomal site in W3110 WT by genome editing | This study |
| W3110 $eutC_{1-20}$-*GFP* | $P_{LtetO-1}$::$eutC_{1-20}$-*GFP* construct inserted at the SS9 safe chromosomal site in W3110 WT by genome editing | This study |
| **Plasmids** | | |
| pCas | *repA101*(Ts), $Kan^R$, $P_{cas}$::*cas9* $P_{araB}$::*Red lacIq* $P_{trc}$::*sgRNA-pMB1* | [22] |
| pTargetF | *pMB1*, $Sp^R$, *sgRNA-acs*; expression of a specific sgRNA to target *acs* in *E. coli* | [22] |
| pTargetF_eut | *pMB1*, $Sp^R$, sgRNA-*eutG*; pTargetF derivative for the expression of a specific sgRNA to target *eutG* in *E. coli* | This study |
| pHD_Δ*eut* | *pUC*, $Amp^R$, contains the 1kb-long upper and lower homology arms required to knock out the chromosomal *eut* operon in W3110 WT | This study |
| pTargetF_SS9 | *pMB1*, $Sp^R$, sgRNA-*SS9*; pTargetF derivative for the expression of a specific sgRNA to target the *SS9* locus in *E. coli* | This study |
| pHD_SS9_eutC-GFP | *pUC*, $Amp^R$, contains 1kb-long homology regions to insert the $P_{LtetO-1}$::*eutC-GFP* construct at the SS9 safe chromosomal site in W3110 WT | This study |
| pHD_SS9_$eutC_{1-20}$-GFP | *pUC*, $Amp^R$, contains 1kb-long homology regions to insert the $P_{LtetO-1}$::$eutC_{1-20}$-*GFP* construct at the SS9 safe chromosomal site in W3110 WT | This study |
| pSEVA661 | *p15A*, $Gm^R$ | [24] |
| pO | $lacI_Q$-$P_{trc}$ cassette and $T_0$ terminator cloned into the multiple cloning site of pSEVA 661 | This study |
| pEut | Entire *eut* operon from W3110 WT cloned into pO under control of $P_{trc}$ | This study |

**Table 1. Bacterial strains and plasmids used in the study.**

| | $\mu_{max}$ ($h^{-1}$) | | | |
|---|---|---|---|---|
| **Strain/Medium** | **M9 glycerol $NH_4Cl$** | **M9 glycerol $NH_4Cl$ IPTG** | **M9 glycerol EA** | **M9 glycerol EA IPTG** |
| WT | 0,37 ± 0,01 | 0,37 ± 0,01 | 0,39 ± 0,01 | 0,39 ± 0,01 |
| Δ*eut* | 0,36 ± 0,03 | 0,35 ± 0,01 | 0,09 ± 0,06 | 0,03 ± 0,02 |
| WT pO | 0,35 ± 0,01 | 0,36 ± 0,01 | 0,38 ± 0,03 | 0,35 ± 0,01 |
| WT pEut | 0,33 ± 0,01 | 0,19 ± 0,01 | 0,37 ± 0,01 | 0,23 ± 0,01 |
| Δeut pO | 0,35 ± 0,01 | 0,35 ± 0,01 | 0,12 ± 0,11 | 0,02 ± 0,01 |
| Δ*eut* pEut | 0,33 ± 0,01 | 0,19 ± 0,01 | 0,37 ± 0,01 | 0,25 ± 0,01 |

**Table 2. Growth of *E. coli* K-12 W3110 strains grown in various M9 medium derivatives.** These experiments were performed using a microplate reader. Data are shown as mean (n = 3 biological replicates) ± standard deviation.

| | Physiological parameters | | | | |
|---|---|---|---|---|---|
| **Medium** | **μ** | **$q_{S)glycerol}$** | **$q_{S)Ethanolamine}$** | **$q_{P)acetate}$** | **$q_{P)ethanol}$** |
| M9 gly $NH_4Cl$ | 0.44 ± 0.02 | 16.2 ± 1.6 | ND | ND | ND |
| M9 gly EA | 0.45 ± 0.01 | 14.7 ± 0.4 | 7.8 ± 0.3 | 1.7 ± 0.1 | 2.6 ± 0.1 |

**Table 3. Growth parameters of *E. coli* K12 W3110 WT grown aerobically in M9 medium containing glycerol as C source and $NH_4Cl$ or EA as N source.** The exponential growth rate μ is expressed in $h^{-1}$; the substrate uptake ($q_S$) and product formation ($q_P$) rates are expressed in mmol.(gDW.h)$^{-1}$. DW: dry weight; ND: not detected. Data are shown as mean (n = 3 biological replicates) ± standard deviation.